Slow-interaction Converter-driven Stability in the Distribution Grid: Small-Signal Stability Analysis with Grid-Following and Grid-Forming Inverters

Arshpreet Singh, Vincent Debusschere, Nouredine Hadjsaid, Xavier Legrand, Benoit Bouzigon

▶ **To cite this version:**

Arshpreet Singh, Vincent Debusschere, Nouredine Hadjsaid, Xavier Legrand, Benoit Bouzigon. Slow-interaction Converter-driven Stability in the Distribution Grid: Small-Signal Stability Analysis with Grid-Following and Grid-Forming Inverters. IEEE Transactions on Power Systems, 2024, 39 (2), pp.4521-4536. 10.1109/TPWRS.2023.3319708 . hal-04227176

HAL Id: hal-04227176
https://hal.science/hal-04227176

Submitted on 3 Oct 2023

HAL is a multi-disciplinary open access archive for the deposit and dissemination of scientific research documents, whether they are published or not. The documents may come from teaching and research institutions in France or abroad, or from public or private research centers.

L'archive ouverte pluridisciplinaire **HAL**, est destinée au dépôt et à la diffusion de documents scientifiques de niveau recherche, publiés ou non, émanant des établissements d'enseignement et de recherche français ou étrangers, des laboratoires publics ou privés.

Slow-interaction Converter-driven Stability in the Distribution Grid: Small-Signal Stability Analysis with Grid-Following and Grid-Forming Inverters

Arshpreet Singh, *Student Member, IEEE,* Vincent Debusschere, *Senior Member, IEEE,* Nouredine Hadjsaid, *Senior Member, IEEE,* Xavier Legrand and Benoit Bouzigon

***Abstract*—Inverter-based resources (IBRs) are changing the dynamics of medium-voltage distribution grids (MVDGs), leading to concerns over slow-interaction converter-driven stability (SICDS). Although researchers have proposed numerous device-level solutions for IBR stability, culminating in the promotion of grid-forming (GFM) as opposed to grid-following (GFL) inverters, a system-level analysis from the point-of-view of the distribution system operator (DSO) is still lacking. As a first step toward standardization, this paper provides some guiding principles for DSOs to prevent SICDS issues in MVDGs, by performing small-signal stability analysis and selecting a set of key parameters from state-of-the-art GFL and GFM models. By imposing bounds for these key parameters, DSOs could manage small-signal interactions between IBRs, as exemplified in the last section of this paper over a 2-IBRs study case, later scaled to a multi-inverter configuration with five inverters in a CIGRE medium voltage distribution benchmark network.**

***Index Terms*—converter-driven stability, small-signal stability, distribution grid stability, grid-following, grid-forming**

I. Introduction

A Growing presence of inverter-based resources (IBRs) is leading distribution system operators (DSOs) to reevaluate their role in power system stability. As stated in [1], a set of new stability issues are gaining prominence in modern power systems, mostly due to a reduction in system inertia, lower contribution to short-circuit currents from IBRs, and interactions between converters; this has resulted in the definition of a new category denominated "converter-driven stability" (CDS), which involves broad instabilities resulting from dynamic interactions between the control systems of IBRs and other devices in the power system.

This category is further subdivided into "fast-interaction CDS" (FICDS) and "slow-interaction CDS" (SICDS), depending on the frequency of the stability issues. In general, FICDS involves harmonic phenomena, with frequencies ranging from hundreds to several thousands of Hz [1]. Although these issues may take system-level proportions, their origin is usually a local resonance involving the output LCL filter of IBRs and their inner current control loops, being mitigated by the addition of active damping mechanisms [2]–[4].

Misters Singh, Debusschere and Hadjsaid are with Univ. Grenoble Alpes, CNRS, Grenoble INP, G2Elab, France.

Misters Legrand and Bouzigon are with Enedis, France.

This work is funded by the Enedis Industrial Chair on Smart Grids.

A. Slow-interaction converter-driven stability (SICDS)

SICDS, on the other hand, involves CDS events with a frequency below 50 Hz [5], including low-frequency oscillations, typically under 10 Hz [1], and subsynchronous control interactions. This issue has been addressed in the literature [5], although studies have mostly focused on micro-grids [6] or large transmission networks, particularly in the context of low inertia [7] and weak grids [8], [9]. Interconnected medium-voltage distribution grids have not been targeted in particular.

While FICDS is highly dependent on local parameters, SICDS may be a result of dynamic interactions between distant IBRs. In other words, while FICDS issues may be solved through careful sizing of passive components and proper tuning of specific control loops during interconnection studies, SICDS issues may take place even when IBRs are well-tuned from the producer's viewpoint. From a DSO's perspective, FICDS issues should be solved at a device level, but SICDS may require system-level actions, such as standardized guidelines for IBRs. Therefore, in the context of medium-voltage (MV) distribution networks, where relatively large IBRs can be connected to the grid (12 MW in France [10]), having a considerable impact on local dynamics, the question of slow-interaction converter-driven stability, in particular, is raising concerns.

Research efforts on SICDS are primarily motivated by real-life events [11], such as the ones observed in Texas [12], Xinjiang [13], and Australia [14]. Considerable literature has been dedicated to explaining such events [8], [9], [15], developing assessment tools for CDS [16], [17], and suggesting control-based solutions [18], especially in the form of grid-forming inverters [19]–[21]. Since the DSO is not usually capable of controlling IBRs directly, however, a different approach may be helpful, aiming instead at providing standardized requirements for decentralized IBRs. In other words, from the point-of-view of DSOs, it may be interesting to move from a device-level to a system-level perspective to address SICDS. This paper represents an effort to fill this gap in the literature, focusing on a DSO-oriented solution to prevent SICDS on MV distribution grids.

This poses a number of challenges, however. First, to provide standardized requirements, the DSO would have to adopt generic models for IBR controllers, which is a difficult task in light of the diversity of control schemes available in the literature. A distinction between two major operation

modes, namely grid-following (GFL) and grid-forming (GFM) inverters, is particularly crucial, since they may have vastly different characteristics with respect to SICDS. Nevertheless, researchers have made considerable progress in recent years toward standardized modeling of IBRs, an overview of which is provided below in Section I-B. A further challenge for the DSO is to find a set of key parameters which can be used as standardized requirements for stability, which we attempt to do via small-signal stability analysis, by proposing such parameters in Sections II-A and II-B, and demonstrating their impact in Section III.

B. Standardized modeling of IBRs: recent developments

Despite the challenge of establishing a unified model for IBR controllers, researchers have made considerable progress in recent years toward the generic modeling of IBRs. In [22], authors have provided a summary on this topic. Most notably, generic models, usually employed in planning studies, are supposed to be vendor-agnostic and should be able to approximately depict the dynamic behavior of IBRs when properly parameterized. For such, these models take advantage of some fundamental building blocks, which are capable of portraying a wide range of behaviors. In GFLs, for instance, these would be the phase-locked loop (PLL) and the inner current control loop; by adding these two components to the preexisting generic models, it is possible to accurately depict SICDS issues in simulations [23], and in small-signal stability analysis [24]. Generic models also exploit some inherent similarities between control methods, such as a Virtual Oscillator Control (VOC) and a PLL [25], or a Power-Synchronization Loop (PSL) and a Virtual Synchronous Machine (VSM) [26]. These similarities allow us to parameterize the models in such a way as to emulate the behavior of different control methods. This is particularly interesting from the point of view of system operators, given that they can establish standardized requirements for a generic control strategy that can be further "translated" onto different control methods.

With respect to GFMs in particular, to unify the wide range of control strategies proposed in the literature, researchers have been suggesting some broad classifications. In [22], there are categories for Droop-based control (DBC) [27], Virtual Synchronous Machine [28], Matching Control (MC) [29], and Virtual Oscillator Control [30]. This is a subject of debate, and this list is not exhaustive, be it because of the existence of other categories (PLL-based GFM, for instance [26]) or due to further similarities between the aforementioned categories, which could lead to a different clustering: a VSM, for example, is a droop-based control with added inertial effect [31], and they can be made equivalent in terms of small-signal stability [32].

These categories are helpful in light of the comparative analyses provided in the literature. For example, EMT implementations led to slight differences in transient behavior in [22], suggesting nonetheless the possibility of unifying the controllers in positive sequence through the parameterization of generic models. For our purposes, however, since we are interested in the assessment of small-signal interactions in a distribution grid with GFMs, the most important conclusions can be taken from [7] and [33]. Mentioning similar categories as [22], the authors of [7] argue that all these strategies lead to equivalent small-signal behavior (an idea that is further elaborated in [34]) and can be thus reduced to a droop-based controller. Focusing specifically on the comparison of such GFM control methods, particularly the "advanced methods" (as presented in [35], namely MC and dispatchable VOC), the authors of [33] concluded that the addition of low-pass filters allows for an equivalent representation of dVOC, VSM, and DBC with respect to their inertial behavior, although they may present discrepancies with respect to damping due to parameterization constraints. In any case, the authors were able to tune these four controllers so as to ensure similar dynamic behavior, which suggests the possibility of using a common droop-based model for representing GFMs in small-signal studies. More research is needed with respect to the generic representation of such advanced control techniques, but they are considered out of the scope of this paper.

Hence, this work aims at delineating some guiding principles for the DSO to prevent SICDS issues in an MV distribution grid. For such, we begin by providing generic IBR models in Section II, synthesizing some of the recent developments on simplified source models, with a special emphasis on photovoltaic solar plants and battery energy storage systems, deriving key control parameters for both grid-following and grid-forming controllers, expressed via intuitive and generalizable indicators such as time responses. A simplified modeling approach for analyzing 2-IBRs systems is also described in this section, being employed in a small-signal stability analysis in Section III, where we summarize some major low-frequency interactions between IBRs. Using sensitivity analysis to define a set of initial parameter ranges in subsection III-A, we define some extreme IBR configurations and assess the stability of scenarios involving their combinations in III-B. These extreme scenarios are then stabilized by improving the bounds of the chosen parameters in subsection III-C. Finally, a case study with five IBRs is presented in subsection III-D, demonstrating the application of the proposed methodology for larger systems.

II. Model description

Our study case consists of two IBRs with $P = 10\,\text{MW}$ connected to a rural MV grid, namely the CIGRE Benchmark European MV Distribution Network [36], shown in Fig. 1, where the network upstream is the Continental European Transmission Grid. Because the interactions between MV-connected IBRs and the network upstream are out of the scope of this paper, we adopt an infinite-bus representation for the high-voltage transmission grid, with short-circuit power $S_{SC} = 5000\,\text{MVA}$ and R/X = 0.1 [36].

A second assumption is that, except for IBRs, the MV network is entirely passive; for simplification, we neglect the dynamics of loads, therefore considered constant-impedance models, as well as on-load tap-changers and capacitor banks, both of which are considerably slower than IBR controllers. It is worth mentioning, however, that local loads may have an impact on CDS: in [37], for instance, a predominance of small

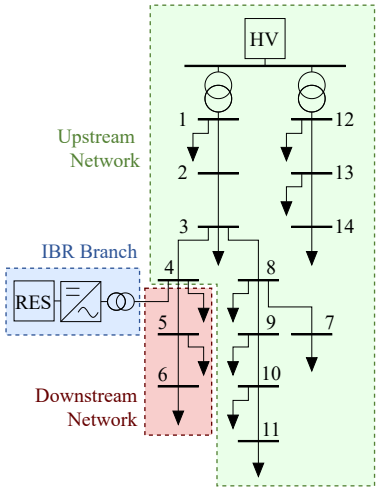

Fig. 1. IBR connected to CIGRE Benchmark European MV Distribution Network, configured for radial operation [36]

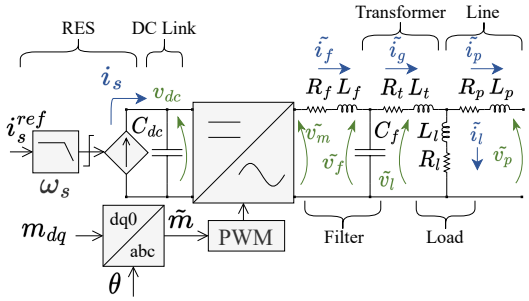

Fig. 2. Physical model of an IBR connected to a MV grid

motors leads to GFMs operating in current limitation mode due to low voltage conditions, affecting their stability. Some specific interactions between IBRs and loads may require advanced load models, such as component-based electromagnetic transient (EMT) models [38]. Since our goal is to study the interaction between IBRs in an isolated manner, load-IBR interactions are considered out of our scope. Moreover, because we are focusing on low-frequency interactions, loads and lines downstream from the IBR point of interconnection (POI) with the grid can be bundled into a single equivalent load, as in a quasi-steady-state model.

Taking these hypotheses into account, the model of an IBR connected to a radial MV grid shown in Fig. 1 can be represented as in Fig. 2.

In its prospective studies for 2050, Enedis, the major French DSO, envisions a RES capacity of up to 275 GW by 2050, most of which (around 84 %) is expected to be in the form of Photovoltaic Solar Power (PV) [39]. Some of these PV plants will presumably be coupled with Battery Energy Storage Systems (BESS). Hence, our renewable energy source (RES) is modeled so as to emulate PV and BESS, disregarding certain source-side stability concerns, which are usually associated with Wind Power Plants (WPP) [40]. Although certain authors might employ a constant DC source for both transient [41] and small-signal analysis [42] of IBRs, or to propose and validate IBR controllers [43], we have opted for a representation that includes the DC-side dynamics, since they may have an impact on small-signal stability [7]. As shown in Fig. 2, we have adopted a controlled current-source model, based on [7], where a first-order delay with a time constant $\tau_s = 1/\omega_s$, in addition to a saturation block, is used to represent the dynamics related to the source-side DC/DC converter. A reference current i_s^{ref} is provided by a Maximum Power Point Tracking (MPPT) algorithm or by the IBR controller. A DC-link capacitor is used as an energy buffer between source and converter. This is a common representation for generic controllable sources, either an energy storage plant or a RES with sufficient headroom, and is commonly employed in the literature [33], [44], [45].

It is worth mentioning that this model may still be useful for representing Type-4 WPPs in certain applications. For instance, authors in [46], aiming to provide a stability assessment for GFMs with limited DC-side current provision, compared this simplified DC-side model with a detailed Type-4 WPP, concluding that the representation is accurate for reproducing v_{dc} instability if the source current limitation is in accordance with the maximum power point of the WPP; otherwise, if this power limitation is not respected, dynamic events could lead the rotor to stall. Moreover, a small-signal stability assessment for offshore WPPs connected to High Voltage Direct Current (HVDC) rectifiers, operating as GFL and GFM, was conducted in [47], arriving at similar conclusions as Section III-C in this paper, namely the key role played by GFL PLL gains and GFM droop constant in the dominant modes of the system. More specifically, for the study of low-frequency dynamics below 10 Hz in WPPs connected to weak grids, it is common for researchers to ignore DC-side dynamics entirely [48], since the root cause of such stability issues can be accurately explained via simplified models.

For the inverter itself, we employ a generalized average model [49]. Writing the network equations for the output filter in per-unit, applying a power-variant *dq0* transformation [50], which uses a phase equal to θ_{ibr} (with an angular speed of ω_{ibr}), provided by the IBR controller, and assuming a balanced three-phase output, we get the set of equations (1)-(3),

$$(L_f/\omega_b)\,\dot{i_{f_d}} = v_{dc}\,m_d - v_{f_d} - R_f\,i_{f_d} + \omega_{ibr}\,L_f\,i_{f_q} \quad (1)$$

$$(L_f/\omega_b)\,\dot{i_{f_q}} = v_{dc}\,m_q - v_{f_q} - R_f\,i_{f_q} - \omega_{ibr}\,L_f\,i_{f_d} \quad (2)$$

$$C_{dc}\,\dot{v_{dc}} = i_s - i_{f_d}\,m_d - i_{f_q}\,m_q \quad (3)$$

where $m_{dq} = \{m_d, m_q\}$ designate the modulation signal $\tilde{m}$ for the PWM, in *dq* frame.

Assuming a LV/MV transformer with no phase-shift and an inductive load, we may represent them using RL circuits, just as the line, for which the capacitances are neglected. These three components forming a "T" will lead to a singularity if all inductor currents are taken as state variables, since their linear combination is equal to zero. In order to avoid this, we may leave $\tilde{i_p}$ aside and take only $i_g = \{i_{g_d}, i_{g_q}\}$ and $i_l = \{i_{l_d}, i_{l_q}\}$ as state variables, obtaining their differential equations by applying a star-delta transformation on the inductances.

It is worth noting that all variables when expressed in *dq* must be referred to the *dq*-frame of the IBR, which is

TABLE I
IBR PHYSICAL PARAMETERS

Parameter	L_f	R_f	C_f	C_{dc}	L_t	R_t	τ_{res}
Value	0.1 pu	0.01 pu	0.1 pu	0.04 pu	0.05 pu	0.0005 pu	1 ms

rotating at ω_{ibr}. An external voltage, such as $\tilde{v_p}$, must be rotated from the global dq-frame, rotating at ω_g, denoted by the superscript "g", to the reference frame of the IBR, using a counterclockwise rotation of $\theta_g - \theta_{ibr}$:

$$\begin{bmatrix} v_{p_d} \\ v_{p_q} \end{bmatrix} = \begin{bmatrix} \cos(\theta_g - \theta_{ibr}) & -\sin(\theta_g - \theta_{ibr}) \\ \sin(\theta_g - \theta_{ibr}) & \cos(\theta_g - \theta_{ibr}) \end{bmatrix} \begin{bmatrix} v_{p_d}^g \\ v_{p_q}^g \end{bmatrix} \quad (4)$$

Hence, the physical model of an IBR branch may be described using a set of differential equations in the form $\dot{x} = f(x, u)$, with state vector x and input vector u:

$$\begin{aligned} x &= \left[i_{f_d}\ i_{f_q}\ v_{dc}\ v_{f_d}\ v_{f_q}\ i_s\ i_{g_d}\ i_{g_q}\ i_{l_d}\ i_{l_q}\right]^\intercal \\ u &= \left[i_s^{ref}\ \ m_d\ m_q\ \theta_{ibr}\ \omega_{ibr}\ v_{p_d}^g\ v_{p_q}^g\ \theta_g\right]^\intercal \end{aligned} \quad (5)$$

Modulation signal $\{m_d, m_q\}$ as well as the phase and frequency of the rotating dq frame $\{\theta_{ibr}, \omega_{ibr}\}$ must be provided by IBR controllers, depending on their operation mode, either GFL or GFM. Parameters required in the physical model of the IBR are given in Table I, where $S_{\text{base}} = 10\,\text{MVA}$, $U_{\text{base}} = 20\,\text{kV}$, and $f_{\text{base}} = 50\,\text{Hz}$.

A. Grid-following control (GFL)

Grid-following inverters are power converters controlled as current sources [51]. They represent most of the IBRs used for integration of RES. GFLs receive commands in terms of active and reactive power, as well as measurements of voltage and current at the POI; their objective is to simply inject P and Q, which, if POI voltage is sufficiently steady, can be done by injecting a certain current $\tilde{i_f}$. This control is ideal for MPPT-based power sources, and for a precise injection of reactive power, which is commonly required in grid codes for voltage support [10].

As shown in Fig. 3, a generic GFL controller is composed of three control loops: internal, external and phase-locked loop (PLL). The standard configuration usually involves a control of active and reactive power, providing current references in a dq frame, which are used in determining a modulation function for the PWM. This dq frame is obtained through a phase-locked loop (PLL), with the purpose of achieving synchronization with the input voltage $\tilde{v_f}$. Q-control is usually done in a direct manner, using a low-pass filter (LPF) for measurements. P-control, on the other hand, may be done in an indirect manner, by controlling v_{dc}; by using this method, a GFL is able to keep v_{dc} under control while injecting whichever power is being provided by the source.

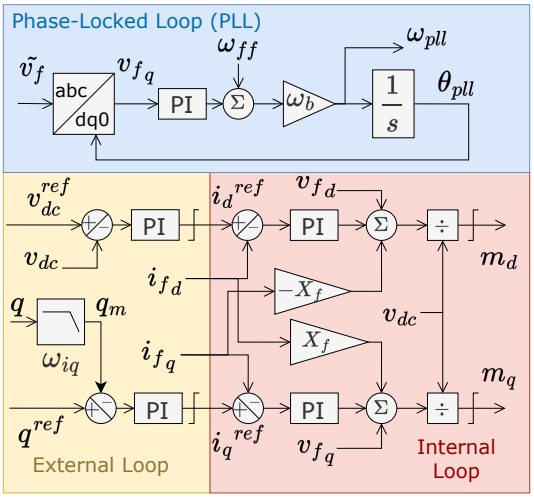

Fig. 3. Control diagram for a Grid-Following Inverter (GFL)

Translating Fig. 3 into differential equations in the form $\dot{x} = f(x, u, z)$, where z is a vector with all algebraic variables, a GFL branch is represented by the following vectors:

$$\begin{aligned} x &= [i_{f_d}\ i_{f_q}\ v_{dc}\ v_{f_d}\ v_{f_q}\ i_s\ i_{g_d}\ i_{g_q}\ i_{l_d}\ i_{l_q} \\ &\qquad \gamma_{v_{dc}}\ q_m\ \gamma_{i_q^{ref}}\ \gamma_{i_{f_d}}\ \gamma_{i_{f_q}}\ \gamma_{pll}\ \theta_{pll}]^\intercal \\ u &= [i_s^{ref}\ {v_{dc}}^{ref}\ q^{ref}\ v_{p_d}^g\ v_{p_q}^g\ \theta_g]^\intercal \\ z &= [m_d\ m_q\ \omega_{pll}]^\intercal \end{aligned} \quad (6)$$

All variables indicated by γ in (6) correspond to integrator outputs in proportional-integral (PI) controllers.

We may also define a vector p with all the parameters related to a GFL branch:

$$\begin{aligned} p = [&\omega_b\ R_f\ L_f\ C_f\ R_t\ L_t\ R_l\ L_l\ R_p\ L_p\ C_{dc}\ \omega_s\ \omega_{ff}\ \omega_{iq} \\ &{K_p}^{vdc}\ {K_i}^{vdc}\ {K_p}^{iq}\ {K_i}^{iq}\ {K_p}^{pll}\ {K_i}^{pll}\ {K_p}^{i}\ {K_i}^{i}]^\intercal \end{aligned} \quad (7)$$

From (7), most non-physical parameters are PI gains K_p and K_i. In order to tune them, one might linearize the model and find approximate first-order open-loop transfer functions in the form of (8),

$$H_p(s) = \frac{K_0}{\tau_0\, s + c_0} \quad (8)$$

where c_0 is either 1 or 0.

If using a PI controller with $H_c(s) = K_p + K_i/s$, we could obtain a closed-loop transfer function by applying (9).

$$H(s) = \frac{N(s)}{D(s)} = \frac{H_p(s)\, H_c(s)}{1 + H_p(s)\, H_c(s)} \quad (9)$$

This leads to a denominator in the form of (10).

$$D(s) = s^2 + 2\,\xi\,\omega_n\, s + \omega_n^2 \quad (10)$$

where ξ is the damping ratio and ω_n is the natural frequency.

Finally, assuming an oscillatory response ($\xi \leq 0.707$), we may obtain a reponse time t_r, or settling time at 5 %, which indicates the time it takes for a step response to reach $\pm 5\,\%$ of its steady-state value, applying (11) [52].

$$t_r \approx \frac{3}{\xi\,\omega_n} \quad (11)$$

TABLE II
GENERIC GFL CONTROLLER TUNING

Description	Open-loop Transfer Function	Tuning Parameter	Gains
Internal Loop	$\frac{v_{dc0}/R_f}{L_f/(\omega_b R_f)\,s+1}$	t_r^i	K_p^i, K_i^i
External Loop: v_{dc}	$\frac{-m_{d0}/C_{dc}}{s}$	$t_r^{v_{dc}}$	$K_p^{v_{dc}}, K_i^{v_{dc}}$
External Loop: q	$\frac{-v_{fd0}}{(1/\omega_{iq})\,s+1}$	$t_r^{i_q}$	$K_p^{i_q}, K_i^{i_q}$
PLL	$\frac{\omega_b}{s}$	t_r^{pll}	K_p^{pll}, K_i^{pll}

TABLE III
STANDARD GFL TUNING PARAMETERS

Parameter	$t_r^{v_{dc}}$	$t_r^{i_q}$	t_r^{pll}	t_r^i	t_r^{qm}	ω_{iq}	ω_{ff}
Value	100 ms	100 ms	50 ms	10 ms	30 ms	33.3 ms	1 pu

With (8)-(11), it is possible to write the gains K_p and K_i as a function of t_r and ξ:

$$K_p = \frac{1}{K_0}\left(\frac{6\,\tau_0}{t_r} - c_0\right) \text{ and } K_i = \frac{9\,\tau_0}{K_0\,\xi^2\,t_r^2} \tag{12}$$

It is a common practice to adopt $\xi = 0.707$, since it usually provides an acceptable trade-off between speed of response and damping of transient oscillations. This is done throughout this paper, reducing our degree of freedom by half for every PI controller. We opt for this approach because we intend to study small-signal stability problems related to interactions between IBRs: a low damping ratio would obviously lead to suboptimal stability, hence it is a conservative assumption to consider this parameter to be properly tuned. Our tuning criteria rely on a desired time-response t_r, which, unlike ξ, is a complex choice.

Table II summarizes the tuning of a generic GFL, while Table III provides the standard tuning parameters adopted in our small-signal stability analysis. Since this paper is focused on low-frequency modes, the tuning vector p_t for a GFL branch may be reduced to three parameters:

$$p_t = [t_r^{v_{dc}}\ t_r^{i_q}\ t_r^{pll}]^\intercal \tag{13}$$

B. Grid-forming control (GFM)

A GFM controller is also composed of an external and internal loop, as seen in Fig. 4, but the primary objective of the latter is to regulate an output voltage $\tilde{v_f}$ instead of a current; hence, a grid-forming inverter is controlled as a voltage source [51]. This can be done either in a direct manner, by controlling the modulation signal $\tilde{m}$ directly from voltage errors [53], or in an indirect manner, by going through a fast current control loop [21]. Because the second method – a cascaded control loop – is generic and representative enough for our purposes, it is adopted throughout this paper.

In microgrids, some GFM applications require IBRs to inject any value of active power, if available, to keep voltage and frequency under control [51]. When multiple GFMs are interconnected, however, this stiff control should be replaced by

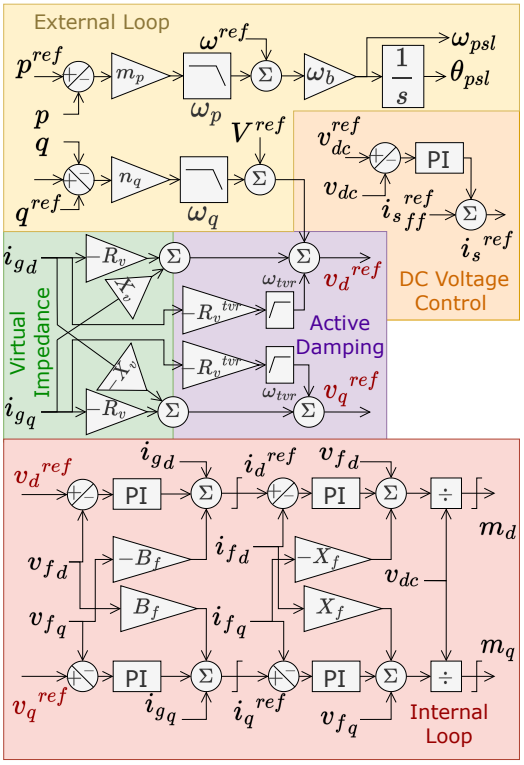

Fig. 4. Control diagram for a Grid-Forming Inverter (GFM)

a droop-based mechanism [27], which emulates a synchronous generator (SG) in its way of sharing power and reacting to power variations via frequency. But SGs react according to a swing equation, due to their rotating mass and its inertial effect when subjected to power imbalances; this leads to slow variations in frequency, which can only be emulated by GFMs if a low-pass filter is added to the droop control, in a method denominated "Virtual Synchronous Machine" [28]. We may thus adapt this control method to ensure a voltage-source behavior and a synchronization capability, in addition to an active power control loop, in what is called a "Power-Synchronization Loop" (PSL) [53].

If the voltage-source is to keep a stiff voltage, we may provide a reference V^{ref} directly to the internal loop. However, multiple additional control features may be integrated to improve the dynamic behavior of the GFM. Most commonly, we may take advantage of this flexibility to add virtual resistances or inductances, either for steady-state corrections, as a Virtual Impedance (VI) [51], or transient improvements, such as a Transient Virtual Resistor (TVR) [53], [54].

Finally, it is worth mentioning that a GFM is not able to comply with any of these control requirements if the DC-link voltage v_{dc} is not kept under control. Since this voltage is sensitive to power imbalances, and active power is already controlled by an external loop, the only way to regulate v_{dc} is via source current i_s. Hence, this source should receive i_s^{ref} from the IBR, which is done by means of a DC voltage control loop. To avoid confusion with the GFL parameter t_r^{vdc}, the tuning parameter for this loop is taken as $\tau_{v_{dc}} = 1/(\xi\,\omega_n)$.

Once again, translating Fig. 4 into differential equations in the form $\dot{x} = f(x, u, z)$, a GFM branch could be represented

by the following vectors:

$$x = [i_{f_d}\ i_{f_q}\ v_{dc}\ v_{f_d}\ v_{f_q}\ i_s\ i_{g_d}\ i_{g_q}\ i_{l_d}\ i_{l_q}\ \gamma_p\ \theta_{psl}\ \gamma_q\ \gamma_{\text{TVR}_d}\ \gamma_{\text{TVR}_q}\ \gamma_{v_{f_d}}\ \gamma_{v_{f_q}}\ \gamma_{i_{f_d}}\ \gamma_{i_{f_q}}\ \gamma_{v_{dc}}]^\intercal$$
$$u = [i_s^{ref}\ p^{ref}\ V^{ref}\ q^{ref}\ {v_{dc}}^{ref}\ \omega^{ref}\ v_{p_d}^{\ g}\ v_{p_q}^{\ g}\ \theta_g]^\intercal \quad (14)$$
$$z = [m_d\ m_q\ \omega_{psl}]^\intercal$$

Variables indicated by γ in (14) correspond to outputs from low-pass filters (γ_p, γ_q), high-pass filters (γ_{TVR_d}, γ_{TVR_q}) or from integrators in PI controllers ($\gamma_{v_{f_d}}$, $\gamma_{v_{f_q}}$, $\gamma_{i_{f_d}}$, $\gamma_{i_{f_q}}$, $\gamma_{v_{dc}}$).

As done for the GFL, we may define a vector p with all the parameters related to a GFM branch:

$$p = [\omega_b\ R_f\ L_f\ C_f\ R_t\ L_t\ R_l\ L_l\ R_p\ L_p\ C_{dc}\ \omega_s\ \omega_{ff}\ \omega_p\ m_p\ \omega_q\ n_q\ \omega_{tvr}\ R_v^{tvr}\ R_v\ X_v\ {K_p}^v\ {K_i}^v\ {K_p}^i\ {K_i}^i\ {K_p}^{vdc}\ {K_i}^{vdc}]^\intercal \quad (15)$$

In order to tune the GFM controller, we ignore the reactive power control loop ($n_q = 0$) for simplification, as well as the additional control loops (VI and TVR), considered out of scope for this paper, since they are not always employed and their tuning is too specific for individual IBRs. Internal control loops can be tuned following the same method as GFLs, and they mostly concern fast interactions. Hence, our focus is on the active power control (APC), which is the most relevant for slow interactions, in addition to the v_{dc} control loop.

APC for GFMs depends on two parameters: droop m_p and LPF cut-off frequency ω_p. If the goal is to achieve synchronization while keeping a transient decoupling between P and Q, as in a power synchronization control [53], we may compute the system time-constant as a function of m_p [54], [55], adopting a droop that provides enough decoupling. In this case, ω_p can be tuned as a regular LPF, to filter out high-frequency noise in P measurements. However, this time-constant depends on external parameters, such as the impedance at the POI, which may not be available to the IBR.

A more generic approach would consist of emulating the swing equation of SGs, tuning the GFM to provide an equivalent inertia H and damping K [28], [56]. Following Fig. 4:

$$\dot{\gamma_p} = -\omega_p\,\gamma_p + \omega_p\,m_p\,(p^{ref} - p) \quad (16)$$

and defining a GFM frequency ω_{psl}, in pu, as:

$$\omega_{psl} = \gamma_p + \omega^{ref} \quad (17)$$

Substituting (17) in (16), we get:

$$2H\,\dot{\omega_{psl}} = p^{ref} - p - K\,(\omega_{psl} - \omega^{ref}) \quad (18)$$

where H and K are defined as in (19).

$$H = \frac{1}{2\,m_p\,\omega_p} \text{ and } K = \frac{1}{m_p} \quad (19)$$

From (18), a PSL-based GFM is capable of emulating the classical swing equation of an SG as expressed in [57], where p^{ref} acts as the mechanical power and ω^{ref} as the rated value of the rotor angular velocity.

Finally, the simplest way to determine m_p is through grid requirements. Since $m_p = \Delta\omega/\Delta p$, for $\Delta p = 1$ pu, a maximum frequency deviation $\Delta\omega$ allowed in most grid codes is around 5 %, so we could adopt an m_p of up to 0.05. With respect to the LPF, it is common to tune it around 5 Hz i.e. $\omega_p = 31.4$ rad/s [56]. In this case, $m_p = 0.01$ leads to a rather low inertia constant $H = 1.6$ in comparison to SGs (4 - 10 [57]). However, there is no consensus about the desirable level of virtual inertia required from IBRs connected to MV networks; for our purposes, rather than sticking to a tuning method in particular, we perform a sensitivity analysis on m_p and ω_p, assessing their impact on small-signal stability.

TABLE IV
STANDARD GFM TUNING PARAMETERS

m_p	ω_p	$\tau_{v_{dc}}$	t_r^v	t_r^i	n_q	ω_q	R_v^{tvr}	ω_{tvr}	R_v	X_v
0.01	31.4 rd/s	5 ms	10 ms	0.5 ms	0	31.4 rd/s	0.028 pu	62.8 rd/s	0	0

With respect to DC voltage control, from the correspondent block represented in Fig. 4 and DC-side equation (3), by linearizing around an equilibrium point, we get:

$$H_p^{v_{dc}}(s) = \frac{\Delta v_{dc}(s)}{\Delta i_s^{ref}(s)} = \frac{\omega_s}{s+\omega_s}\,\frac{1/C_{dc}}{s} \quad (20)$$

In order to simplify our tuning, we may consider an approximation which is only valid if the source is relatively fast with respect to the time-response of this control loop: $\tau_s = 1/\omega_s << \tau_{v_{dc}}$. In the case of PVs, this delay is usually under a millisecond. Since we intend to take $\tau_{v_{dc}}$ in the order of at least a few milliseconds, we may apply this approximation, reducing (20) to $H_p^{v_{dc}}(s) = \frac{1/C_{dc}}{s}$; this allows us to apply (12), bringing down the DC voltage control to a single parameter: $\tau_{v_{dc}}$.

Table IV provides the standard GFM tuning parameters adopted in our studies. As for the GFL, tuning vector p_t for a GFM branch may also be reduced to three parameters:

$$p_t = [m_p\ \omega_p\ \tau_{v_{dc}}]^\intercal \quad (21)$$

C. Global state-space with multiple IBRs

Each IBR branch as well as the upstream network can be described by a set of non-linear differential equations f, algebraic equations g, and output equations h. Denoting the i^{th} element, either an IBR branch or the upstream network, by the subscript i, we may write:

$$\begin{aligned} \dot{x_i} &= f_i(x_i, u_i, z_i) \\ 0 &= g_i(x_i, u_i, z_i) \\ y_i &= h_i(x_i, u_i, z_i) \end{aligned} \quad (22)$$

Linearizing around an equilibrium point x_{i0}, for which $\dot{x_i} = f_i(x_{i0}, u_{i0}, z_{i0}) = 0$, we may rewrite (22) as (23):

$$\begin{aligned} \Delta\dot{x_i} &= A_i\,\Delta x_i + B_i\,\Delta u_i \\ \Delta y_i &= C_i\,\Delta x_i + D_i\,\Delta u_i \end{aligned} \quad (23)$$

where A_i, B_i, C_i, and D_i are jacobian matrices representing this element as a state-space.

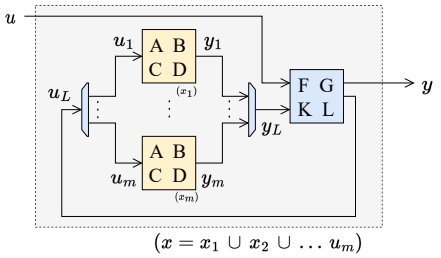

Fig. 5. Association of multiple state-spaces into a single state-space

Taking all m elements in the system, $\forall i \in [1, m]$, we may group them as a unique state-space, which may be written in an open-loop form, hereby denoted by subscript "L":

$$\begin{aligned} \Delta\dot{x}_L &= A_L\,\Delta x_L + B_L\,\Delta u_L \\ \Delta y_L &= C_L\,\Delta x_L + D_L\,\Delta u_L \end{aligned} \tag{24}$$

where A_L, B_L, C_L, and D_L are diagonal concatenations of individual matrices A_i, B_i, C_i, and D_i, respectively; similarly, x_L, u_L, and y_L are vertical concatenations of the individual state, input, and output vectors, respectively.

Evidently, all states must be included into the global state-space: $\Delta x = \Delta x_L$. Open-loop input vector Δu_L and closed-loop output vector Δy may be written as a function of global input vector Δu and open-loop Δy_L, as shown in Fig. 5 and expressed below:

$$\begin{aligned} \Delta u_L &= F\,\Delta u + G\,\Delta y_L \\ \Delta y &= K\,\Delta u + L\,\Delta y_L \end{aligned} \tag{25}$$

Taking (24) and (25), we derive a closed-loop state-space:

$$\begin{aligned} \Delta\dot{x} &= A\,\Delta x + B\,\Delta u \\ \Delta y &= C\,\Delta x + D\,\Delta u \end{aligned} \tag{26}$$

Considering $E_L = (I - D_l\,G)^{-1}$, closed-loop matrices A, B, C, and D may be computed as:

$$\begin{aligned} A &= A_L + B_L\,G\,E_L\,C_L & C &= L\,E_L\,C_L \\ B &= (B_L\,G\,E_L\,D_L + B_L)\,F & D &= L\,E_L\,D_L\,F + K \end{aligned} \tag{27}$$

D. Obtaining the state matrix "A" for our study case

In order to build a global state-space for our study case, we consider a generic number of n IBR branches, all of which are connected at a common node, which also includes the upstream network, as in Fig. 6.

Here, for each IBR branch k, $k \in [1, n]$, we have:

$$u_k = [({u_k}^s)^\intercal\ \ (u^g)^\intercal]^\intercal \text{ and } y_k = [({i_k}^g)^\intercal\ \ ({v_k}^g)^\intercal]^\intercal \tag{28}$$

where the k$^{\text{th}}$ input vector u_k is subdivided into two components: setpoint vector u_k^s, unique for each IBR, according to its operation mode (GFL or GFM), and grid input vector u^g, same for all IBR branches. For convenience, output vector y_k may also be subdivided into a current vector i_k^g and a voltage vector v_k^g. All of these are described below:

$$\begin{aligned} u_k^s &= \left[{i_s}^{ref}\ \ {v_{dc}}^{ref}\ \ q^{ref}\right]^\intercal, \text{ if GFL} \\ u_k^s &= \left[{i_s}^{ref}\ \ p^{ref}\ \ V^{ref}\ \ q^{ref}\ \ {v_{dc}}^{ref}\right]^\intercal, \text{ if GFM} \\ u^g &= \left[{v_p}_d^g\ \ {v_p}_q^g\ \ \theta_g\right]^\intercal;\ \ i_k^g = \left[{i_p}_{dk}^g\ \ {i_p}_{q_k}^g\right]^\intercal;\ \ v_k^g = \left[{v_l}_{dk}^g\ \ {v_l}_{q_k}^g\right]^\intercal \end{aligned} \tag{29}$$

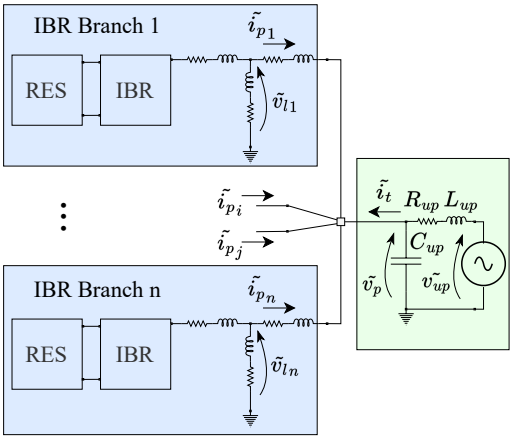

Fig. 6. Multiple IBR branches connected to a single-bus representation of the upstream network

A similar representation may be adopted for the upstream network:

$$u_{up} = \left[(u_{up}^s)^\intercal\ \ (u_{up}^g)^\intercal\right]^\intercal \text{ and } y_{up} = \left[{v_p}_d^g\ \ {v_p}_q^g\ \ \theta_g\right]^\intercal \tag{30}$$

where:

$$u_{up}^s = [\omega_g\ \ V_{up}]^\intercal \text{ and } u_{up}^g = \left[{i_t}_d^g\ \ {i_t}_q^g\right]^\intercal$$

It is possible to obtain u_{up}^g as a function of output currents i_k^g by applying Kirchhoff's first law to the common node:

$${i_t}_d^g = -\sum_{k=1}^{n} {i_p}_{dk}^g \text{ and } {i_t}_q^g = -\sum_{k=1}^{n} {i_p}_{q_k}^g \tag{31}$$

We may thus rewrite u_{up}^g as:

$$u_{up}^g = -\left[\begin{pmatrix}1&0&0&0\\0&1&0&0\end{pmatrix}\ \cdots\ \begin{pmatrix}1&0&0&0\\0&1&0&0\end{pmatrix}\right]\begin{bmatrix}\begin{pmatrix}{i_p}_{d1}^g\\{i_p}_{q1}^g\\{v_l}_{d1}^g\\{v_l}_{q1}^g\end{pmatrix}\\\vdots\\y_n\end{bmatrix}$$

which, denoting "I" for identity matrices, gives:

$$u_{up}^g = [\,(-I\ \ 0)\ \ \ldots\ \ (-I\ \ 0)\,]\,[y_1^\intercal\ \ \ldots\ \ y_n^\intercal]^\intercal \tag{32}$$

Hence, there is a relation between IBR inputs and upstream outputs, namely $u^g = y_{up}$, as well as a relation between IBR outputs and upstream inputs, expressed in (32). Adding to these the differential and algebraic equations from each state-space, and linearizing them around an equilibrium point, we may write down an open-loop state-space formulation of the global system according to (24), where, for subscripts "1" to "n" designating IBR branches and "up" designating the upstream network,

$$\begin{aligned} \Delta x_L &= \left[\Delta x_1^\intercal\ \ \ldots\ \ \Delta x_n^\intercal\ \ \Delta x_{up}^\intercal\right]^\intercal \\ \Delta u_L &= \left[\Delta u_1^\intercal\ \ \ldots\ \ \Delta u_n^\intercal\ \ \Delta u_{up}^\intercal\right]^\intercal \\ \Delta y_L &= \left[\Delta y_1^\intercal\ \ \ldots\ \ \Delta y_n^\intercal\ \ \Delta y_{up}^\intercal\right]^\intercal \end{aligned} \tag{33}$$

For IBR branch 1, we may express Δu_1 as:

$$\Delta u_1 = \begin{bmatrix} I & 0 & \dots & 0 \\ 0 & 0 & \dots & 0 \end{bmatrix} \begin{bmatrix} \Delta u_1^s \\ \vdots \\ \Delta u_n^s \\ \Delta u_{up}^s \end{bmatrix} + \begin{bmatrix} 0 & \dots & 0 & 0 \\ 0 & \dots & 0 & I \end{bmatrix} \begin{bmatrix} \Delta y_1 \\ \vdots \\ \Delta y_n \\ \Delta y_{up} \end{bmatrix} \quad (34)$$

Similarly, for the upstream, we may rewrite Δu_{up} as:

$$\Delta u_{up} = \begin{bmatrix} \Delta u_{up}^s \\ \Delta u_{up}^g \end{bmatrix} = F_{up} \begin{bmatrix} \Delta u_1^s \\ \vdots \\ \Delta u_n^s \\ \Delta u_{up}^s \end{bmatrix} + G_{up} \begin{bmatrix} \Delta y_1 \\ \vdots \\ \Delta y_n \\ \Delta y_{up} \end{bmatrix} \quad (35)$$

where, computing Δu_{up}^g from (32),

$$F_{up} = \begin{bmatrix} 0 & \dots & 0 & I \\ 0 & \dots & 0 & 0 \end{bmatrix}, G_{up} = \begin{bmatrix} (0\ 0) & \dots & (0\ 0) & (0\ 0) \\ (-I\ 0) & \dots & (-I\ 0) & (0\ 0) \end{bmatrix}$$

Generalizing (34) for n IBRs and grouping it with (35):

$$\begin{bmatrix} \Delta u_1 \\ \vdots \\ \Delta u_n \\ \Delta u_{up} \end{bmatrix} = F \begin{bmatrix} \Delta u_1^s \\ \vdots \\ \Delta u_n^s \\ \Delta u_{up}^s \end{bmatrix} + G \begin{bmatrix} \Delta y_1 \\ \vdots \\ \Delta y_n \\ \Delta y_{up} \end{bmatrix} \quad (36)$$

where:

$$F = \begin{bmatrix} I & 0 & \dots & 0 & 0 \\ 0 & 0 & \dots & 0 & 0 \\ \vdots & \vdots & \ddots & \vdots & \vdots \\ 0 & 0 & \dots & I & 0 \\ 0 & 0 & \dots & 0 & 0 \\ 0 & 0 & \dots & 0 & I \\ 0 & 0 & \dots & 0 & 0 \end{bmatrix}, \quad G = \begin{bmatrix} 0 & \dots & 0 & 0 \\ 0 & \dots & 0 & I \\ \vdots & \vdots & \vdots & \vdots \\ 0 & \dots & 0 & 0 \\ 0 & \dots & 0 & I \\ (0\ 0) & \dots & (0\ 0) & (0\ 0) \\ (-I\ 0) & \dots & (-I\ 0) & (0\ 0) \end{bmatrix}$$

As we can see, (36) is in the form $\Delta u_L = F\,\Delta u + G\,\Delta y_L$ (25), where closed-loop input vector u assembles all setpoints in the system:

$$u = [\, u_1^s \ \dots \ u_n^s \ \ u_{up}^s \,]^\intercal \quad (37)$$

Given that we have F and G from (36), we may obtain the state-matrix A using (27).

It is worth noting that the simplified modeling approach described in subsection II-C is only valid in some particular situations, such as a multi-IBR configuration where each one of them is connected to a different feeder or a configuration with multiple IBRs connected to the same node in the distribution grid. In our case, in particular, as we intend to dive deeper into a configuration with two IBRs connected to the network from Fig. 1, the representation from Fig. 6 with $n = 2$ could serve our purposes. A generic representation could be obtained without simplifications by following the steps described in [58].

III. Small signal stability analysis

Using the state matrix A obtained in the last section, it is possible to perform a small-signal stability analysis (SSSA) for an MV grid with IBRs [57], which is done by computing the eigenvalues of A, hereby noted as "λ". SSSA is a classical method to evaluate the stability of equilibrium points in dynamic systems, linearizing its dynamic equations around these equilibrium points and studying the eigenvalues of the resulting state matrix. In traditional SG-dominated power systems, SSSA measures the ability of the system to maintain synchronism when subjected to small disturbances [57]. In practice, SSSA has been mostly used for detecting insufficient damping of power oscillations, which are mitigated through power systems stabilizers (PSS) but has also found applications in voltage stability and subsynchronous resonance analysis. In recent years, applications of SSSA have been extended to power-electronic-dominated systems [7], being adapted into frequency-domain and impedance-based methods, and being employed in model order reduction techniques [59].

For our purposes, SSSA serves as an instrument for assessing interactions between IBRs; we may employ classical tools, such as eigen-sensitivity and participation factors, to detect the modes by which IBRs interact with each other and the key parameters that could be tuned for mitigating oscillations and instabilities. The main difference is that, instead of focusing on the tuning of a given IBR for dynamic purposes, we are trying to find adequate ranges for key parameters in a multi-IBR setting so as to ensure system-level small-signal stability, which could be a practical methodology for a DSO.

Following the hypotheses presented in Section II, which reduces the system from Fig. 1 to Fig. 6, where each IBR is represented as in Fig. 2, we first select some scenarios of interest, presented in Table V, chosen to reflect realistic conditions with respect to POI strength and distance between IBRs.

For the remainder of this paper, our system consists of two IBRs, either GFL or GFM, connected to a common upstream network via lines and loads as indicated in Table VI. This table represents the steady-state equivalent of Table V taking both IBRs as GFMs. Scenarios S3-S4 involve nodes further away from the substation when compared to scenarios S1-S2, hence the former is taken as weak grid scenarios, while the latter will designate a strong grid. Scenarios S1-S3 involve short distances between IBRs i.e below 1 km; S2-S4, on the other hand, comprise IBRs distant from each other.

TABLE V
Selected scenarios for small-signal stability analysis

Scenario	Node IBR 1	Node IBR 2	Distance IBR 1-2
S1	3	4	0.8 km
S2	3	5	1.4 km
S3	10	11	0.5 km
S4	7	11	3.3 km

TABLE VI
Equivalent representation of IBRs for selected scenarios

	SCR Up.	R/X Up.	X_{line} [pu] IBR 1	R/X$_{\text{line}}$ IBR 1	X_{line} [pu] IBR 2	R/X$_{\text{line}}$ IBR 2	$\overline{S}_{\text{load}}$ [pu] IBR 1	$\overline{S}_{\text{load}}$ [pu] IBR 2
S1	4.77	0.40	0.0018	0.70	0.0127	0.70	$0.75\angle 0.6°$	$0.26\angle 7.7°$
S2	4.77	0.40	0.0018	0.70	0.0228	0.70	$0.80\angle 0.7°$	$0.20\angle 8.9°$
S3	3.76	0.42	0.0018	0.70	0.0077	0.70	$0.67\angle 2.3°$	$0.18\angle 3.8°$
S4	4.14	0.40	0.0322	0.68	0.0277	0.68	$0.37\angle 1.2°$	$0.50\angle 3.6°$

TABLE VII
SUMMARY OF SMALL-SIGNAL SENSITIVITY ANALYSIS FOR CHOSEN TUNING PARAMETERS

IBR	Par.	Range	Worst Scen.	Worst Config.	Worst Par. Value	Max. $\Re(\lambda)$	Freq. for Max. $\Re(\lambda)$
GFL	$t_r^{v_{dc}}$	$50-220$ ms	S3	GFL/GFM	220 ms	-1.1	2.6 Hz
GFL	$t_r^{i_q}$	$50-1000$ ms	S4	GFL/GFL	1000 ms	-2.4	0.6 Hz
GFL	t_r^{pll}	$20-1000$ ms	S2	GFL/GFM	1000 ms	-3.0	0.5 Hz
GFM	m_p	$0.005-0.045$	S3	GFM/GFM	0.045	-1.5	11.4 Hz
GFM	ω_p	$2.5-50$ rd/s	S1,S2	GFM/GFL	2.5 rd/s	-1.2	0.9 Hz
GFM	$\tau_{v_{dc}}$	$3-70$ ms	S1-S4	GFM/GFL	70 ms	-1.5	3.3 Hz

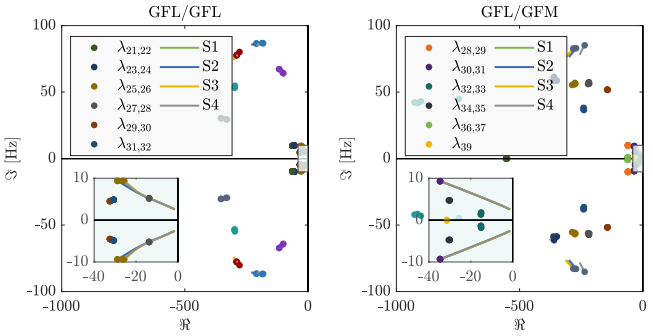

Fig. 7. Small-signal sensitivity for a 2-IBRs configuration, where $t_r^{v_{dc}}$ for IBR 1 (GFL) is taken from 50 to 220 ms. Initial eigenvalues are indicated by the circles, where $t_r^{v_{dc}} = 50$ ms; they evolve along the scenarios {S1-S4} as $t_r^{v_{dc}}$ increases.

A. Sensitivities

In order to assess the impact of key parameters, given in (13) and (21), we may perform a sensitivity analysis and observe the behavior of dominant modes. Assuming that both IBRs are initially tuned according to their standard configuration, as in Tables III and IV, a single parameter from IBR 1 varies along the range presented in Table VII, while IBR 2 rests unaltered. Table VII also summarizes the results for this sensitivity analysis: within the chosen ranges, all parameters may drive the dominant mode, or the eigenvalue with maximum real part ($\max \Re(\lambda)$), relatively close to the imaginary axis; frequencies for these modes are between 0.5 and 11.4 Hz. For illustration, two interesting cases are presented below.

From Fig. 7, it is possible to see how high values of $t_r^{v_{dc}}$ may lead to weakly-damped low-frequency oscillations. For both configurations, all scenarios converge when $t_r^{v_{dc}}$ is high, which suggests that this form of instability is unrelated to grid conditions. Although both configurations present similar results, GFL/GFM is slightly worse than GFL/GFL, as can be observed through the time-domain simulations presented in Fig. 8: if IBR 2 is a GFM, it will present power oscillations due to a badly-tuned parameter in IBR 1, constituting an undesirable small-signal interaction.

Fig. 9 presents the sensitivity for the droop constant m_p in IBR 1, which is now a GFM. This time, there is a visible discrepancy between scenarios and configurations. Nearby IBRs, with one of them reaching high droop levels (close to 0.045), will interact through weakly-damped oscillations; in this case, a weak grid configuration with distant IBRs (Scenario S4) is

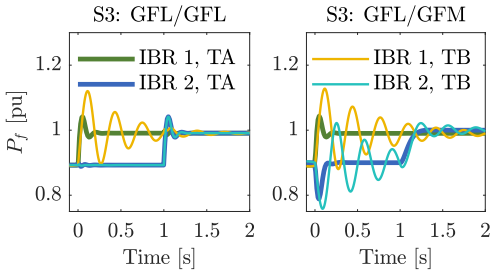

Fig. 8. Time-domain simulation to illustrate the results from Fig. 7. Here, "IBR 1" and "IBR 2" represent the injected power P_f for each inverter, following a 0.1 pu step on p^{ref} for IBR 1 (at $t = 0$ s) and IBR 2 ($t = 1$ s). "TA" and "TB" are tuning configurations: "TA" is the standard configuration ($t_r^{v_{dc}} = 100$ ms for both IBRs), whereas "TB" presents a modified tuning for IBR 1: $t_r^{v_{dc}} = 220$ ms.

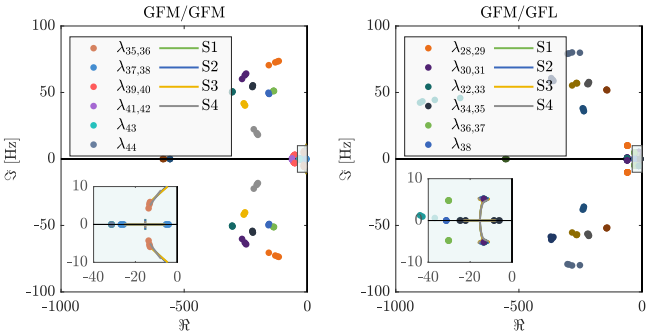

Fig. 9. Small-signal sensitivity for a 2-IBRs configuration, where m_p for IBR 1 (GFM) is taken from 0.005 to 0.045.

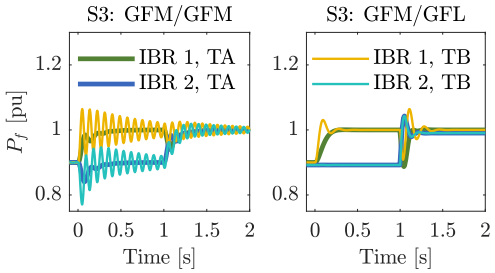

Fig. 10. Time-domain simulation to illustrate the results from Fig. 9. P_f for both IBRs following a 0.1 pu step on p^{ref} for IBR 1 (at $t = 0$ s) and IBR 2 ($t = 1$ s). Once again, "TA" is the standard tuning configuration ($m_p = 0.01$ for both IBRs), while "TB" is modified for IBR 1: $m_p = 0.045$.

less prone to instability. It is interesting to notice that switching IBR 2 from GFM to GFL leads to a configuration that is considerably more stable, as shown in Fig. 10.

B. Extreme IBR configurations

From the point of view of the DSO, knowing that a set of key parameters can reproduce the most relevant low-frequency interactions between IBRs, it is crucial to define and assess worst-case scenarios. The objective is for the DSO to provide bounds for these parameters, ascertaining that even the worst combination between bound values will not lead to unstable situations. Our study-case consists of two IBRs, either GFL or GFM, each having three key parameters; considering the four scenarios we have taken into account, if each parameter is to assume a bound value, either minimum or maximum,

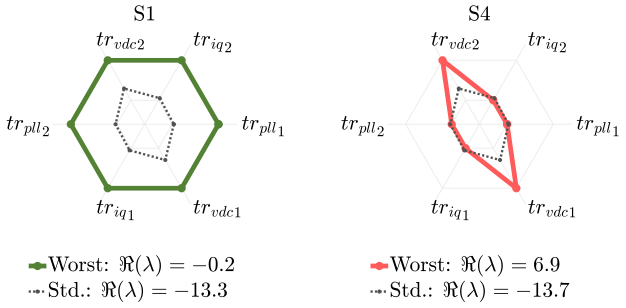

Fig. 11. Worst combination between bound values for a GFL/GFL configuration, for scenarios S1 and S4. In this case, S2 and S3 can be omitted, since they present the same structure as S1 and S4, respectively, while their corresponding worst case is less extreme. $\Re(\lambda)$ indicates the maximum real part among all eigenvalues computed for these combinations.

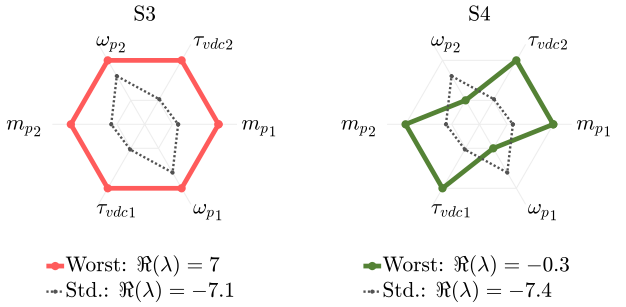

Fig. 12. Worst combination between bound values for a GFM/GFM configuration, for scenarios S3-S4. Here, S1 and S2 can be omitted, since both of them present the same structure as S3.

each IBR configuration would involve 256 possibilities, all scenarios comprised. The first step is to select the parameter combinations among all these possibilities that lead to the worst situations in terms of small-signal stability. For such, the initial bounds are taken as the ranges presented in Table VII.

Through this analysis, we observe that the worst situations take place for IBR configurations of the type GFL/GFL, shown in Fig. 11, and GFM/GFM, shown in Fig. 12. These figures indicate a given parameter combination: outer hexagons indicate the upper bound values for each parameter, normalized, while inner hexagons refer to the lower bounds, and dashed lines are the standard values (Tables III, IV).

Hence, there are two additional GFL and GFM configurations that should be taken into account for assessing worst-case scenarios, as summarized in Table VIII. Two specific parameter combinations may even lead to instability. In a GFL/GFL configuration, for scenario S4 (distant IBRs connected to a weak grid), with both GFLs configured as "GFLC" from Table VIII, Fig. 11 indicates an instability. Similarly, a GFM/GFM in scenario S3 (nearby IBRs), with both GFMs configured as "GFMB", would also lead to instability, as shown in Fig. 12.

Taking into account these two additional GFL and GFM parameter configurations given in Table VIII, which me may designate as "extreme configurations", in addition to the standard ones, henceforth denominated GFLA and GFLB, it

TABLE VIII
EXTREME IBR CONFIGURATIONS

Par.	GFLA	GFLB	GFLC	Par.	GFMA	GFMB	GFMC
$t_r^{v_{dc}}$	100 ms	220 ms	220 ms	m_p	0.01	0.045	0.045
t_r^{iq}	100 ms	1000 ms	1000 ms	ω_p	31.4 rd/s	50 rd/s	2.5 rd/s
t_r^{pll}	50 ms	1000 ms	20 ms	$\tau_{v_{dc}}$	5 ms	70 ms	70 ms

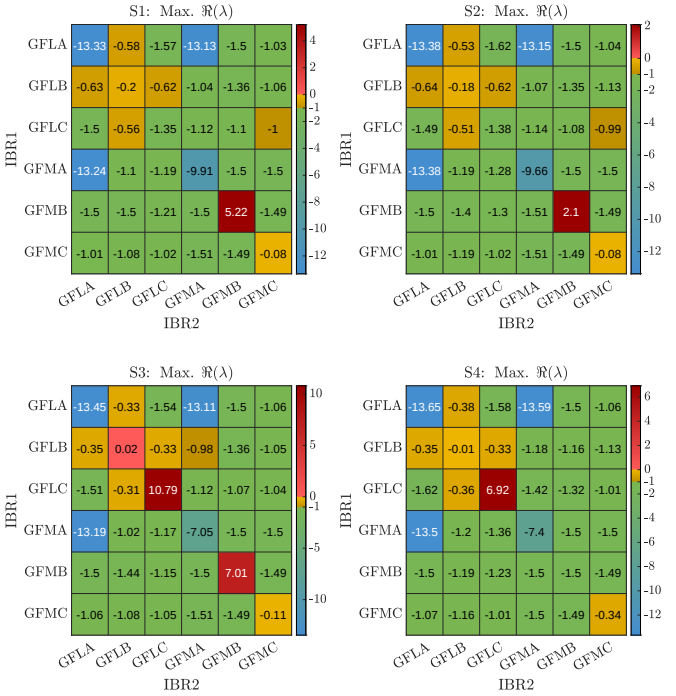

Fig. 13. Combinations between a set of IBR configurations, for all scenarios (S1-S4). Each square represents the maximum real part among all eigenvalues for the correspondent combination between IBR1 and IBR2.

is possible to visualize a large number of stability scenarios.

Fig. 13 provides this visualization and a number of conclusions: as expected, standard configurations are considerably more stable than the other ones; GFMB/GFMB, which is a high-droop configuration, leads to instability for all scenarios expect for S4 (distant IBRs connected to weak grids); on the other hand, GFLC/GFLC, a fast-PLL configuration, leads to instability only under weak grids (scenarios S3 and S4). GFLB leads to weak damping in all scenarios, becoming slightly unstable in S3. GFMC/GFMC, characterized by slow v_{dc} control, also leads to damping issues in all scenarios.

C. Improving parameter bounds for stability

From Fig. 13, it is clear that the initial parameter bounds given in Table VII are unable to ensure small-signal stability under the stringent configurations presented in Table VIII. To improve these bounds, we may perform some additional sensitivity studies for S3, worst scenario according to Fig. 13.

1) Fast-PLL instability: Since GFLC/GFLC is defined by a fast PLL, we may perform a sensitivity analysis on t_r^{pll}, trying to find the value that would lead to an acceptable $\max \Re(\lambda)$ (close to -1, for instance). This time, t_r^{pll} is modified

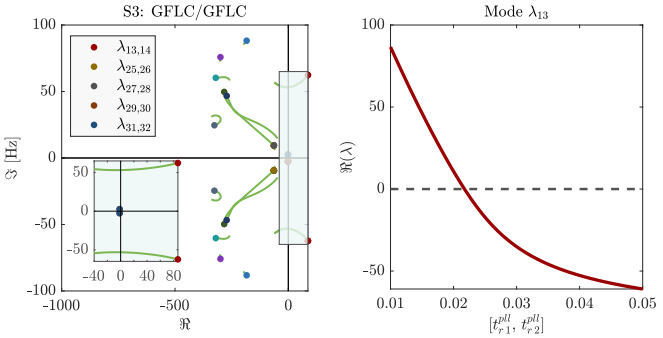

(a) Small-signal sensitivity (b) Eigenvalue trajectory

Fig. 14. Small-signal sensitivity for a 2-IBRs configuration, where t_r^{pll} for both IBR 1 and IBR 2 is taken from 10 to 50 ms. Both IBRs are GFLs configured as "GFLC", hence with $t_r^{v_{dc}} = \max(t_r^{v_{dc}})$ and $t_r^{i_q} = \min(t_r^{i_q})$.

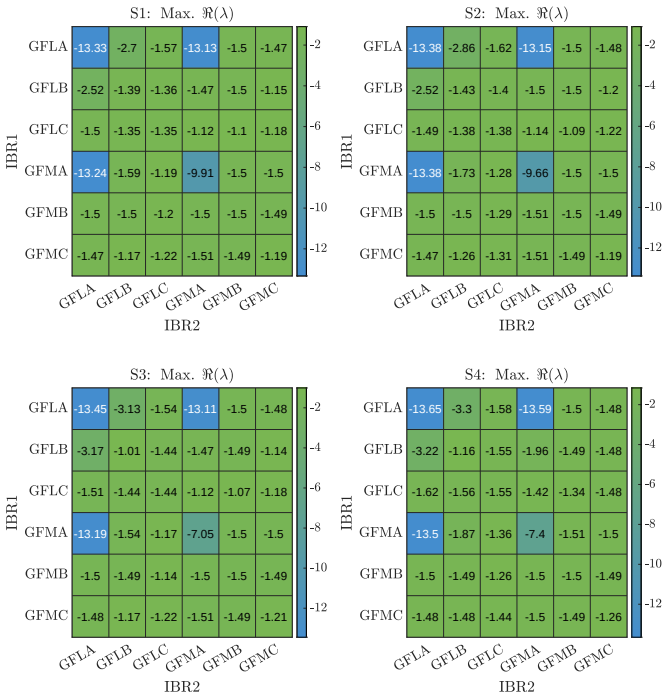

Fig. 15. Combinations between a set of IBR configurations, for all scenarios (S1-S4), considering a new set of bound values for the key tuning parameters, presented in Table IX.

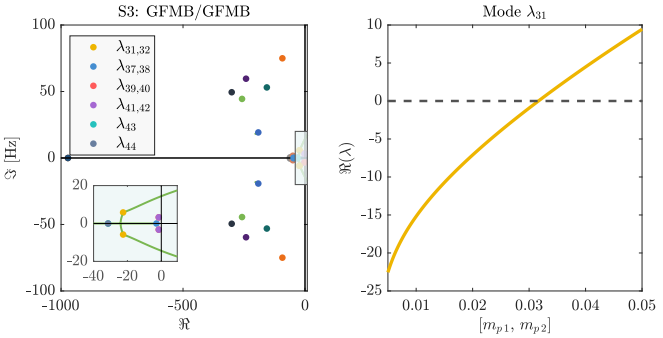

(a) Small-signal sensitivity (b) Eigenvalue trajectory

Fig. 16. Small-signal sensitivity for a 2-IBRs configuration, where m_p for both IBR 1 and IBR 2 is taken from 0.005 to 0.05. Both IBRs are GFMs configured as "GFMB", hence with $\omega_p = \max(\omega_p)$ and $\tau^{v_{dc}} = \max(\tau^{v_{dc}})$.

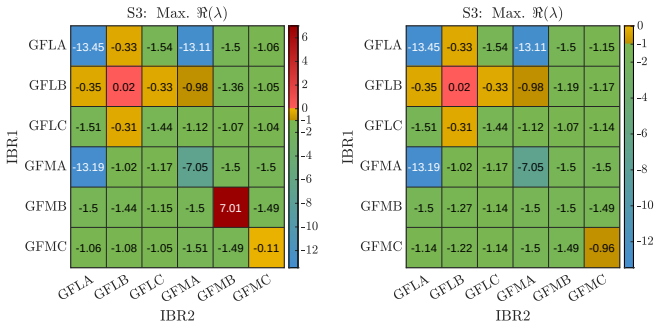

(a) Stabilizing GFLC/GFLC (b) Stabilizing GFMB/GFMB

Fig. 17. Combinations between a set of IBR configurations for scenario S3. In Fig. 17a, we consider an increase in the lower bound of t_r^{pll}, which is now $t_r^{pll} = 25$ ms, eliminating the instability for combination GFLC/GFLC. Fig 17b considers a subsequent decrease in the upper bound of m_p, which becomes $m_p = 0.025$, eliminating the instability for GFMB/GFMB.

TABLE IX
IMPROVED BOUNDS FOR KEY TUNING PARAMETERS

IBR	Parameter	Minimum	Maximum	Standard
GFL	$t_r^{v_{dc}}$	50 ms	220 ms	100 ms
	$t_r^{i_q}$	50 ms	400 ms	100 ms
	t_r^{pll}	25 ms	300 ms	50 ms
GFM	m_p	0.005	0.025	0.01
	ω_p	5 rd/s	50 rd/s	31.4 rd/s
	$\tau_{v_{dc}}$	3 ms	70 ms	5 ms

for both IBRs at the same time, as shown in Fig. 14. We observe that increasing the minimum t_r^{pll} to 25 ms leads to $\max \Re(\lambda) = -1.44$, which eliminates the instability, as can be seen in Fig. 17a.

2) High-droop instability: A similar procedure can be followed to solve a GFMB/GFMB instability, mostly related to an elevated droop constant m_p. Resorting once more to a sensitivity study, Fig. 16 indicates that reducing the maximum m_p down to 0.025 eliminates this instability. Once again, Fig. 17b corroborates this conclusion, demonstrating a further improvement with respect to Fig. 17a.

3) Improved bounds: The remaining parameters can also be improved, culminating in the values given in Table IX. These new bounds lead to an updated situation with respect to combinations between extreme configurations, as shown in Fig. 15. Compared to Fig. 13, all instabilities have been eliminated, as well as low damping situations with $\max \Re(\lambda) < -1$.

Using well-known tools, namely a small-signal stability analysis, the DSO is able to provide improved bounds for a set of key parameters to prevent SICDS problems.

D. Multi-inverters case study: 5 IBRs connected to the MV network

In order to provide an illustration of this methodology in a more complex system, we may repeat the previous steps from Section II-C for a configuration with five IBRs connected to the network from Fig. 1 according to Table X. This scenario is particularly interesting for our purposes since GFLs are connected to the weakest nodes, while GFMs are connected to the

TABLE X
SELECTED SCENARIO FOR FIVE IBRS

IBR	IBR 1	IBR 2	IBR 3	IBR 4	IBR 5
Type	GFM	GFM	GFL	GFL	GFL
Node	3	4	7	10	11

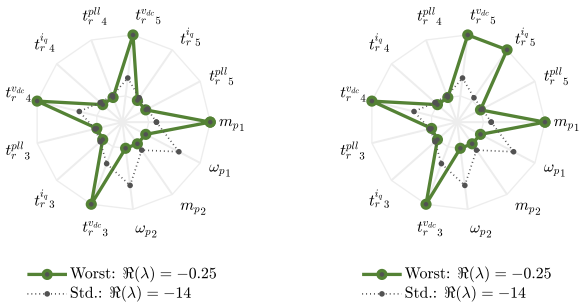

Fig. 18. Two worst combinations between bound values for the selected 5-IBRs scenario.

strongest nodes and in proximity to each other, constituting a worst-case scenario with respect to this specific configuration. To keep a reasonable ratio between generation and load, the total load of the network is raised to 5 pu, which is equal to the total power provided by the IBRs. Moreover, unlike the previous example with two IBRs, it would be unreasonable to explore every single IBR combination, hence we will keep the GFMs and GFLs connected to the same nodes. In the previous example, we intended to understand the physical origin of interactions between IBRs in general, while in a scenario with more IBRs the goal is more practical, e.g., to evaluate the interactions in this specific configuration, as well as the proper actions to take regarding the limits of the key parameters. We are assuming that, in practice, DSOs will know which IBRs are configured as GFLs or GFMs, hence they will not have to examine all possible configurations.

For simplicity, since our previous example showed little impact of $\tau_{v_{dc}}$, this parameter is omitted in this example, GFMs are assessed in terms of m_p and ω_p exclusively. Adopting the same initial bounds as in Table VII and repeating the sensitivity analysis from Subsection III-A, we do not find any unstable scenario within these ranges, hence we may use the same bound values to obtain the extreme configurations. This time, none of these configurations leads to instability, although some situations with low damping may take place. In Fig. 18, we observe the two scenarios with the highest Max. $\Re(\lambda)$, which are close to zero, but not yet unstable. The lack of unstable situations is not a surprise, since the 2-IBRs example already hinted at better stability for scenarios with a GFL-GFM mix, as was shown in Fig. 13.

For a system with five IBRs, most scenarios with high Max. $\Re(\lambda)$ happen for the IBR settings described in Table XI. Note that, since there are two GFMs with two parameters each and three GFLs with three parameters each, we have a total of four possible configurations for GFM and eight for GFL,

TABLE XI
EXTREME IBR CONFIGURATIONS FOR FIVE IBRS

Par.	GFLB	GFLC	GFLD	Par.	GFMB	GFMC
$t_r^{v_{dc}}$	220 ms	220 ms	220 ms	m_p	0.005	0.045
$t_r^{i_q}$	50 ms	50 ms	1000 ms	ω_p	2.5 rd/s	2.5 rd/s
t_r^{pll}	20 ms	1000 ms	20 ms			

TABLE XII
SELECTED COMBINATIONS BETWEEN A SET OF IBR CONFIGURATIONS

Comb.	Max. $\Re(\lambda)$	Freq. for Max. $\Re(\lambda)$	IBR 1	IBR 2	IBR 3	IBR 4	IBR 5
1	-0.25	3.17 Hz	GFMC	GFMB	GFLB	GFLB	GFLB
2	-0.98	3.10 Hz	GFMB	GFMC	GFLD	GFLD	GFLD
3	-1.32	0.47 Hz	GFMB	GFMB	GFLC	GFLC	GFLC
4	-1.42	3.00 Hz	GFMC	GFMC	GFLC	GFLC	GFLC

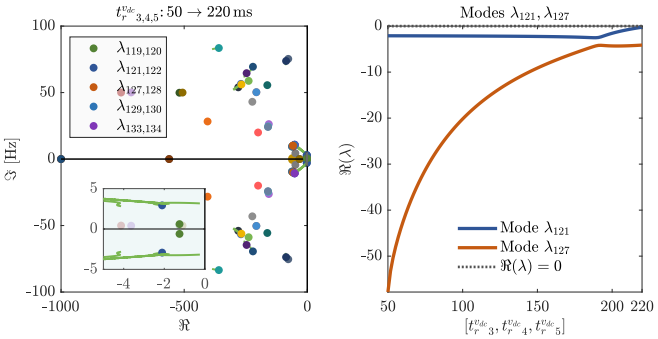

(a) Small-signal sensitivity (b) Eigenvalue trajectory

Fig. 19. Small-signal sensitivity for a 5-IBRs configuration, where $t_r^{v_{dc}}$ for IBR 3, 4 and 5 is taken from 50 to 220 ms. All GFLs are configured as "GFLB", while IBR 1 is a GFMC and IBR 2 is a GFMB, as described in the first row of Table XII.

considering that in each extreme configuration, every parameter is either at its lower or upper bound. However, picking five among these twelve possibilities is enough to represent the worst situations, reducing the problem's complexity.

The next step is to combine these IBR configurations. However, unlike in Subsection III-B, where these combinations could be visualized in a matrix (see Fig. 13), we cannot resort to such representations in a 5-dimensional problem. Some of the combinations are displayed in Table XII, revealing how the worst situation arrives in a particular setup with two slow-acting GFMs, one with a high droop (GFMC) and one with a low droop (GFMB), as well as a GFL with slow v_{dc} control (GFLB). This suggests that ω_p and $t_r^{v_{dc}}$ might play a major role in this combination, which we can confirm via sensitivity analysis and participation factors.

Fig. 19 presents the sensitivity of two low-frequency modes, λ_{121} and λ_{127}, to $t_r^{v_{dc}}$. When this GFL time-response is too slow, namely above 200 ms, these modes tend to approach the imaginary axis, leading to a low-damping scenario. It is interesting to observe, however, that mode λ_{127} is also impacted by the GFM parameter ω_p, as illustrated in Fig. 20. This has an interesting implication for DSOs, given that a SICDS issue originated by slow-acting GFLs could actually

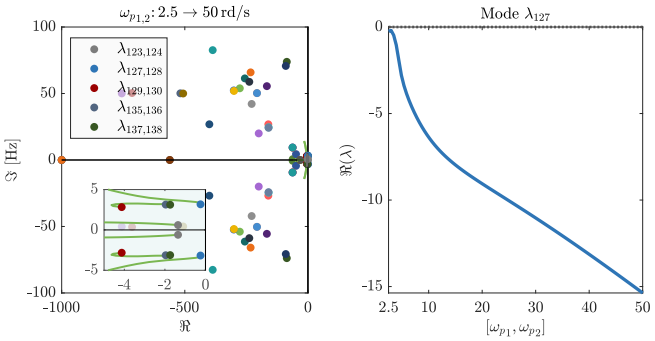

(a) Small-signal sensitivity (b) Eigenvalue trajectory

Fig. 20. Small-signal sensitivity for a 5-IBRs configuration, where ω_p for IBR 1 and 2 is taken from 2.5 to 50 rd/s. All other IBRs are configured as in Fig. 19.

TABLE XIII
SELECTED COMBINATIONS AFTER BOUND IMPROVEMENT

Comb.	Max. $\Re(\lambda)$	Freq. for Max. $\Re(\lambda)$	IBR 1	IBR 2	IBR 3	IBR 4	IBR 5
1	−2.19	4.10 Hz	GFMC	GFMB	GFLB	GFLB	GFLB
2	−2.59	0.55 Hz	GFMB	GFMC	GFLD	GFLD	GFLD
3	−2.63	0.59 Hz	GFMB	GFMB	GFLC	GFLC	GFLC
4	−1.38	3.21 Hz	GFMC	GFMC	GFLC	GFLC	GFLC

be resolved by tuning a distant GFM.

Fig. 21 may further elucidate this interaction. Participation factors for λ_{127} clearly indicate an interaction between the three GFLs and the first GFM (connected to Node 3) for this scenario, while the participation of IBR 2 (a low-droop GFM connected to Node 4) is negligible. For both types of IBRs, the predominant states are related to the active power control: v_{dc} and $\gamma_{v_{dc}}$ for GFLs, θ and γ_p for GFMs.

Considerable improvement may be thus achieved by acting on the bounds of $t_r^{v_{dc}}$ and ω_p, as can be inferred from Fig. 19 and Fig. 20. Decreasing the maximum $t_r^{v_{dc}}$ to 200 ms and increasing the minimum ω_p to 5 rd/s, the combinations presented in Table XII will present lower Max. $\Re(\lambda)$, as indicated in Table XIII. Once again, the worst of these combinations is illustrated through time-domain simulations in Fig. 22. A small disturbance in IBR 3 (0.1 pu increase in the power reference p^{ref}) leads to oscillations in two distant GFMs. Re-tuning the two key parameters considerably reduces these oscillations.

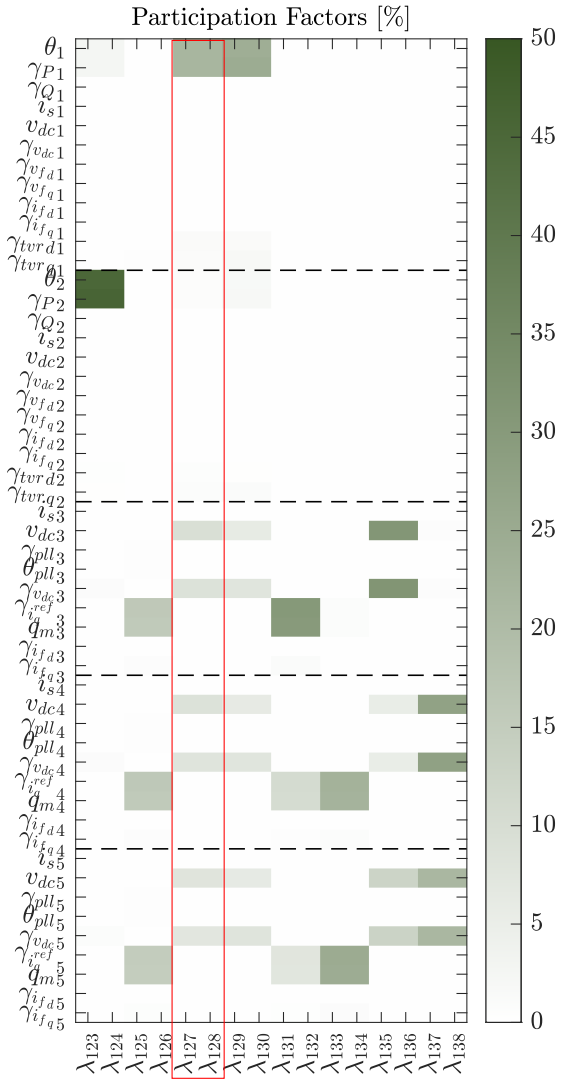

Fig. 21. Participation factors for the combination described in the first row of Table XII. For better visualization, all the states related to inner loops or grid variables have been omitted. The red square highlights an interaction between the three GFLs and the first GFM while the participation of IBR 2 is negligible (as pointed out in the text).

IV. Conclusions

This work was aimed at providing guiding principles to prevent slow-interaction converter-driven stability (SICDS) issues in MV distribution grids. First, a set of key parameters were defined for both grid-following (GFL) and grid-forming (GFM) inverters, having their initial bounds determined by small-signal sensitivities. After selecting some extreme inverter-based resource (IBR) configurations, some of which led to instability, these bounds were modified to ensure small-signal stability.

In conclusion, following the same steps, a distribution system operator can prevent SICDS problems in an MV distribution grid with GFL and/or GFM inverters. Since all scenarios presented in this paper were extracted from a benchmark network, while the IBRs were configured in compliance with the French grid code, our analysis relies on realistic situations and could serve as an initial step toward standardized requirements for IBRs to avoid SICDS issues. This has been detailed on a 2-IBRs configuration and expanded on a 5-IBRs study case, with similar conclusions.

Further work is still necessary, however, regarding a more thorough and scalable method to automatically obtain generic bounds for key parameters in grids with a high number of IBRs, possibly resorting to optimization algorithms. A more complex analysis could also include the interactions between MV-connected IBRs and local loads, or between an active

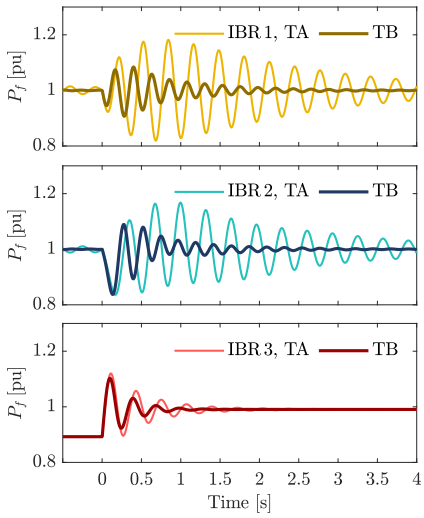

Fig. 22. Time-domain simulation to illustrate the results from Fig. 19 and Fig. 20. Here we observe the injected power P_f for inverters "IBR 1", "IBR 2' and "IBR 3", following a 0.1 pu step on p^{ref} for IBR 3 (at $t = 0$ s). Other IBRs are omitted. "TA" and "TB" are different configurations, although both of them represent the worst IBR combination in Table XII: "TA" is the configuration before updating the bounds ($t_r^{vdc} = 220$ ms for all GFLs and $\omega_p = 2.5$ rd/s for all GFMs), whereas "TB" presents an improved configuration, with $t_r^{vdc} = 200$ ms and $\omega_p = 5$ rd/s.

MV grid and the network upstream, particularly in the case of low inertia.

REFERENCES

[1] N. Hatziargyriou, J. Milanovic, C. Rahmann, V. Ajjarapu, C. Canizares, I. Erlich, D. Hill, I. Hiskens, I. Kamwa, B. Pal, P. Pourbeik, J. Sanchez-Gasca, A. Stankovic, T. Van Cutsem, V. Vittal, and C. Vournas, "Definition and Classification of Power System Stability – Revisited Extended," *IEEE Transactions on Power Systems*, vol. 36, no. 4, pp. 3271–3281, 2021.

[2] X. Wang and F. Blaabjerg, "Harmonic Stability in Power Electronic-Based Power Systems: Concept, Modeling, and Analysis," *IEEE Transactions on Smart Grid*, vol. 10, no. 3, pp. 2858–2870, 2019.

[3] E. Ebrahimzadeh, F. Blaabjerg, X. Wang, and C. L. Bak, "Harmonic Stability and Resonance Analysis in Large PMSG-Based Wind Power Plants," *IEEE Transactions on Sustainable Energy*, vol. 9, no. 1, pp. 12–23, 2018.

[4] M. Lu, Y. Yang, B. Johnson, and F. Blaabjerg, "An Interaction-Admittance Model for Multi-Inverter Grid-Connected Systems," *IEEE Transactions on Power Electronics*, vol. 34, no. 8, pp. 7542–7557, 2019.

[5] L. Kong, Y. Xue, L. Qiao, and F. Wang, "Review of Small-Signal Converter-Driven Stability Issues in Power Systems," *IEEE Open Access Journal of Power and Energy*, vol. 9, pp. 29–41, 2022.

[6] M. Farrokhabadi, C. A. Cañizares, J. W. Simpson-Porco, E. Nasr, L. Fan, P. A. Mendoza-Araya, R. Tonkoski, U. Tamrakar, N. Hatziargyriou, D. Lagos, R. W. Wies, M. Paolone, M. Liserre, L. Meegahapola, M. Kabalan, A. H. Hajimiragha, D. Peralta, M. A. Elizondo, K. P. Schneider, F. K. Tuffner, and J. Reilly, "Microgrid Stability Definitions, Analysis, and Examples," *IEEE Transactions on Power Systems*, vol. 35, no. 1, pp. 13–29, 2020.

[7] U. Markovic, O. Stanojev, P. Aristidou, E. Vrettos, D. Callaway, and G. Hug, "Understanding Small-Signal Stability of Low-Inertia Systems," *IEEE Transactions on Power Systems*, vol. 36, no. 5, pp. 3997–4017, 2021.

[8] L. Fan and Z. Miao, "An Explanation of Oscillations Due to Wind Power Plants Weak Grid Interconnection," *IEEE Transactions on Sustainable Energy*, vol. 9, no. 1, pp. 488–490, 2018.

[9] Y. Li, L. Fan, and Z. Miao, "Wind in Weak Grids: Low-Frequency Oscillations, Subsynchronous Oscillations, and Torsional Interactions," *IEEE Transactions on Power Systems*, vol. 35, no. 1, pp. 109–118, 2020.

[10] Enedis, "Principle and Conditions for Implementing Local Reactive Power Control for Generation Facilities Connected to the HV Public Distribution Network, in French (Principe et Conditions de Mise en Œuvre d'une Régulation Locale de Puissance Réactive pour les Installations de Production Raccordées au Réseau Public de Distribution HTA)," *Enedis NOI - RES 60*, 2016.

[11] Y. Cheng, L. Fan, J. Rose, S.-H. Huang, J. Schmall, X. Wang, X. Xie, J. Shair, J. R. Ramamurthy, N. Modi, C. Li, C. Wang, S. Shah, B. Pal, Z. Miao, A. Isaacs, J. Mahseredjian, and J. Zhou, "Real-World Subsynchronous Oscillation Events in Power Grids With High Penetrations of Inverter-Based Resources," *IEEE Transactions on Power Systems*, vol. 38, no. 1, pp. 316–330, 2023.

[12] S.-H. Huang, J. Schmall, J. Conto, J. Adams, Y. Zhang, and C. Carter, "Voltage Control Challenges on Weak Grids with High Penetration of Wind Generation: ERCOT Experience," in *IEEE Power & Energy Society General Meeting (PES-GM)*, pp. 1–7, 2012.

[13] H. Liu, X. Xie, J. He, T. Xu, Z. Yu, C. Wang, and C. Zhang, "Subsynchronous Interaction Between Direct-Drive PMSG Based Wind Farms and Weak AC Networks," *IEEE Transactions on Power Systems*, vol. 32, no. 6, pp. 4708–4720, 2017.

[14] E. Farahani, P. F. Mayer, J. Tan, F. Spescha, and M. Gordon, "Oscillatory Interaction between Large Scale IBR and Synchronous Generators in the NEM," *CIGRE Science & Engineering*, vol. 28, no. March, pp. 170–183, 2023.

[15] Y. Li, L. Fan, and Z. Miao, "Replicating Real-World Wind Farm SSR Events," *IEEE Transactions on Power Delivery*, vol. 35, no. 1, pp. 339–348, 2020.

[16] L. Fan and Z. Miao, "Admittance-Based Stability Analysis: Bode Plots, Nyquist Diagrams or Eigenvalue Analysis?," *IEEE Transactions on Power Systems*, vol. 35, no. 4, pp. 3312–3315, 2020.

[17] X. Wang, L. Harnefors, and F. Blaabjerg, "Unified Impedance Model of Grid-Connected Voltage-Source Converters," *IEEE Transactions on Power Electronics*, vol. 33, no. 2, pp. 1775–1787, 2018.

[18] Y. Li, L. Fan, and Z. Miao, "Stability Control for Wind in Weak Grids," *IEEE Transactions on Sustainable Energy*, vol. 10, no. 4, pp. 2094–2103, 2019.

[19] J. Matevosyan, J. MacDowell, N. Miller, B. Badrzadeh, D. Ramasubramanian, A. Isaacs, R. Quint, E. Quitmann, R. Pfeiffer, H. Urdal, T. Prevost, V. Vittal, D. Woodford, S. H. Huang, and J. O'Sullivan, "A Future With Inverter-Based Resources: Finding Strength From Traditional Weakness," *IEEE Power and Energy Magazine*, vol. 19, no. 6, pp. 18–28, 2021.

[20] J. Matevosyan, B. Badrzadeh, T. Prevost, E. Quitmann, D. Ramasubramanian, H. Urdal, S. Achilles, J. MacDowell, S. H. Huang, V. Vital, J. O'Sullivan, and R. Quint, "Grid-Forming Inverters: Are They the Key for High Renewable Penetration?," *IEEE Power and Energy Magazine*, vol. 17, no. 6, pp. 89–98, 2019.

[21] T. Qoria, E. Rokrok, A. Bruyere, B. François, and X. Guillaud, "A PLL-Free Grid-Forming Control With Decoupled Functionalities for High-Power Transmission System Applications," *IEEE Access*, vol. 8, pp. 197363–197378, 2020.

[22] EPRI, "Grid Forming Inverters: Tutorial," tech. rep., EPRI, Palo Alto, CA, 2022. 3002025483.

[23] D. Ramasubramanian, W. Wang, P. Pourbeik, E. Farantatos, A. Gaikwad, S. Soni, and V. Chadliev, "Positive sequence voltage source converter mathematical model for use in low short circuit systems," *IET Generation, Transmission & Distribution*, vol. 14, no. 1, pp. 87–97, 2020.

[24] A. Singh, V. Debusschere, and N. Hadjsaid, "Slow-interaction Converter-driven Stability in the Distribution Grid: Small Signal Stability Analysis using RMS Models," in *IEEE Power & Energy Society General Meeting (PES-GM)*, pp. 1–5, 2022.

[25] D. Ramasubramanian and E. Farantatos, "Representation of Grid Forming Virtual Oscillator Controller Dynamics with WECC Generic Models," in *IEEE Power & Energy Society General Meeting (PES-GM)*, pp. 1–5, 2021.

[26] E. Rokrok, T. Qoria, A. Bruyere, B. Francois, and X. Guillaud, "Classification and Dynamic Assessment of Droop-Based Grid-Forming Control Schemes: Application in HVDC Systems," *Electric Power Systems Research*, vol. 189, p. 106765, 2020.

[27] M. C. Chandorkar, D. M. Divan, and R. Adapa, "Control of Parallel Connected Inverters in Standalone Ac Supply Systems," *IEEE Transactions on Industry Applications*, vol. 29, no. 1, pp. 136–143, 1993.

[28] J. Liu, Y. Miura, H. Bevrani, and T. Ise, "Enhanced Virtual Synchronous Generator Control for Parallel Inverters in Microgrids," *IEEE Transactions on Smart Grid*, vol. 8, no. 5, pp. 2268–2277, 2017.

[29] C. Arghir and F. Dörfler, "The Electronic Realization of Synchronous Machines: Model Matching, Angle Tracking, and Energy Shaping

Techniques," *IEEE Transactions on Power Electronics*, vol. 35, no. 4, pp. 4398–4410, 2020.
[30] G.-S. Seo, M. Colombino, I. Subotic, B. Johnson, D. Groß, and F. Dörfler, "Dispatchable Virtual Oscillator Control for Decentralized Inverter-dominated Power Systems: Analysis and Experiments," in *IEEE Applied Power Electronics Conference and Exposition (APEC)*, pp. 561–566, 2019.
[31] J. Liu, Y. Miura, and T. Ise, "Comparison of Dynamic Characteristics Between Virtual Synchronous Generator and Droop Control in Inverter-Based Distributed Generators," *IEEE Transactions on Power Electronics*, vol. 31, no. 5, pp. 3600–3611, 2016.
[32] S. D'Arco and J. A. Suul, "Equivalence of Virtual Synchronous Machines and Frequency-Droops for Converter-Based MicroGrids," *IEEE Transactions on Smart Grid*, vol. 5, no. 1, pp. 394–395, 2014.
[33] D. A. Aragon, E. Unamuno, S. Ceballos, and J. A. Barrena, "Comparative Small-Signal Evaluation of Advanced Grid-Forming Control Techniques," *Electric Power Systems Research*, vol. 211, p. 108154, 2022.
[34] D. Groß, M. Colombino, J.-S. Brouillon, and F. Dörfler, "The Effect of Transmission-Line Dynamics on Grid-Forming Dispatchable Virtual Oscillator Control," *IEEE Transactions on Control of Network Systems*, vol. 6, no. 3, pp. 1148–1160, 2019.
[35] T. Jouini, U. Markovic, and D. Groß, "Deliverable D3.3 - New Options for Existing System Services and Needs for New System Services," tech. rep., Migrate EU H2020, Dec. 2018.
[36] K. Strunz, E. Abbasi, R. Fletcher, N. Hatziargyriou, R. Iravani, and G. Joos, *TF C6.04.02 : TB 575 – Benchmark Systems for Network Integration of Renewable and Distributed Energy Resources*. CIGRE, Apr. 2014.
[37] P. Mitra, L. Sundaresh, and D. Ramasubramanian, "Stability of Inverter-Based Resource (IBR) Dominated Systems with Different Types of Local Loads," *CIGRE Science & Engineering*, vol. 28, no. March, pp. 5–24, 2023.
[38] M. Torabi Milani, B. Khodabakhchian, J. Mahseredjian, and K. Sheshyekani, "Development and Validation of a New Detailed EMT-Type Component-Based Load Model," *Electric Power Systems Research*, vol. 197, p. 107290, 2021.
[39] Enedis, "Prospective Elements for the Public Electricity Distribution Network in 2050, in French (Eléments De Prospective Du Réseau Public De Distribution D'Électricité À L'Horizon 2050)," tech. rep., Enedis, 2021.
[40] D. Xie, Y. Lu, J. Sun, and C. Gu, "Small-Signal Stability Analysis for Different Types of PMSGs Connected to the Grid," *Renewable Energy*, vol. 106, pp. 149–164, 2017.
[41] T. Qoria, F. Gruson, F. Colas, G. Denis, T. Prevost, and X. Guillaud, "Critical Clearing Time Determination and Enhancement of Grid-Forming Converters Embedding Virtual Impedance As Current Limitation Algorithm," *IEEE Journal of Emerging and Selected Topics in Power Electronics*, vol. 8, no. 2, pp. 1050–1061, 2019.
[42] R. Liu, L. Ding, C. Xue, and Y. R. Li, "Small-signal modelling and analysis of microgrids with synchronous and virtual synchronous generators," *IET Energy Systems Integration*, vol. n/a, no. n/a.
[43] D. B. Rathnayake, R. Razzaghi, and B. Bahrani, "Generalized Virtual Synchronous Generator Control Design for Renewable Power Systems," *IEEE Transactions on Sustainable Energy*, vol. 13, no. 2, pp. 1021–1036, 2022.
[44] O. Stanojev, U. Markovic, P. Aristidou, and G. Hug, "Improving Stability of Low-Inertia Systems using Virtual Induction Machine Synchronization for Grid-Following Converters," *IEEE Transactions on Power Systems*, 2022.
[45] A. Tayyebi, D. Groß, A. Anta, F. Kupzog, and F. Dörfler, "Frequency Stability of Synchronous Machines and Grid-Forming Power Converters," *IEEE Journal of Emerging and Selected Topics in Power Electronics*, vol. 8, no. 2, pp. 1004–1018, 2020.
[46] S. Samanta and N. R. Chaudhuri, "Stability Analysis of Grid-Forming Converters Under DC-Side Current Limitation in Primary Frequency Response Regime," *IEEE Transactions on Power Systems*, vol. 37, no. 4, pp. 3077–3091, 2022.
[47] J. Martínez-Turégano, S. Añó-Villalba, S. Bernal-Perez, R. Peña, and R. Blasco-Gimenez, "Small-Signal Stability and Fault Performance of Mixed Grid Forming and Grid Following Offshore Wind Power Plants Connected to a HVDC-Diode Rectifier," *IET Renewable Power Generation*, vol. 14, no. 12, pp. 2166–2175, 2020.
[48] L. Fan, "Modeling Type-4 Wind in Weak Grids," *IEEE Transactions on Sustainable Energy*, vol. 10, no. 2, pp. 853–864, 2019.
[49] S. Bacha, I. Munteanu, and A. I. Bratcu, *Power Electronic Converters Modeling and Control - with Case Studies*. Advanced Textbooks in Control and Signal Processing, Springer, Sept. 2013.
[50] D. Baimel, J. Belikov, J. M. Guerrero, and Y. Levron, "Dynamic Modeling of Networks, Microgrids, and Renewable Sources in the dq0 Reference Frame: A Survey," *IEEE Access*, vol. 5, pp. 21323–21335, 2017.
[51] J. Rocabert, A. Luna, F. Blaabjerg, and P. Rodríguez, "Control of Power Converters in AC Microgrids," *IEEE Transactions on Power Electronics*, vol. 27, no. 11, pp. 4734–4749, 2012.
[52] M. A. Haidekker, "6 - a Tale of Two Poles: The Positioner Example and the Significance of the Poles in the S-Plane," in *Linear Feedback Controls (Second Edition)* (M. A. Haidekker, ed.), pp. 87–108, Elsevier, second edition ed., 2020.
[53] L. Zhang, L. Harnefors, and H.-P. Nee, "Power-Synchronization Control of Grid-Connected Voltage-Source Converters," *IEEE Transactions on Power Systems*, vol. 25, no. 2, pp. 809–820, 2010.
[54] L. Zhang, L. Harnefors, and H.-P. Nee, "Interconnection of Two Very Weak AC Systems by VSC-HVDC Links Using Power-Synchronization Control," *IEEE Transactions on Power Systems*, vol. 26, no. 1, pp. 344–355, 2011.
[55] T. Qoria, *Grid-Forming Control to Achieve a 100 % Power Electronics Interfaced Power Transmission Systems*. Theses, HESAM Université, Nov. 2020.
[56] T. Qoria, Q. Cossart, L. Chuanye, X. Guillaud, F. Colas, F. Grusen, and X. Kestelyn, "Local Control and Simulation Tools for Large Transmission Systems," tech. rep., Migrate 2020 Deliverable D3.2, Dec. 2018.
[57] P. Kundur, N. J. Balu, and M. G. Lauby, *Power System Stability and Control*. EPRI Power System Engineering Series, McGraw-Hill Education, 1994.
[58] N. Pogaku, M. Prodanovic, and T. C. Green, "Modeling, Analysis and Testing of Autonomous Operation of an Inverter-Based Microgrid," *IEEE Transactions on Power Electronics*, vol. 22, no. 2, pp. 613–625, 2007.
[59] M. Cheah-Mane, A. Egea-Alvarez, E. Prieto-Araujo, H. Mehrjerdi, O. Gomis-Bellmunt, and L. Xu, "Modeling and Analysis Approaches for Small-Signal Stability Assessment of Power-Electronic-Dominated Systems," *WIREs Energy and Environment*, vol. 12, no. 1, p. e453, 2023.

Arshpreet Singh (StM'21) received his B.S. degree in Electrical Engineering from the University of São Paulo, Brazil, and his M.S. degree in Electric Power Systems from the Grenoble Institute of Technology (Grenoble-INP), University Grenoble Alpes, France, in 2019. Since 2020, he has been a Ph.D. candidate with the Electrical Engineering Laboratory G2ELab, Grenoble-INP, studying the stability of distribution grids with high penetration of renewable energy sources, as part of the Enedis Industrial Chair on Smart Grids.

Vincent Debusschere (M'11–SM'21) received the B.S. and M.S. degrees in applied physics from the (now) University of Paris-Saclay in 2004 and the Ph.D. degree in electrical engineering from the Ecole Normale Supérieure de Cachan, Rennes, France, in 2009. Since 2010, he has been an Associate Professor with the Electrical Engineering Laboratory G2ELab, Grenoble Institute of Technology, University Grenoble Alpes. He is the author of more than 120 articles. His research interests concern electric power systems with a specific focus on modeling and optimization for operation and planning, multi-criteria design of energy systems including energy communities, and application of machine learning algorithms to energy systems. He is an Associate Editor of the journal Sustainability and holds four patents.

Nouredine Hadjsaid (SM) received the Ph.D. and "Habilitation à Diriger des Recherches" degrees in 1992 and 1998, respectively, from the Grenoble Institute of Technology (Grenoble-INP), University Grenoble Alpes, France, where he is currently a Full Professor. He is also affiliated with Nanyang Technological University (NTU), Singapore, while serving as director in the Electrical Engineering Laboratory G2ELab and as a visiting professor at Virginia Tech, USA. His research focuses on smart grids, which include distributed generation, information and communication technologies, and grid security and stability, among other topics. He is the former treasurer and incumbent vice president for new initiatives and outreach in the IEEE Power & Energy Society.

Xavier Legrand received the M.S. degree in electrical engineering from National Institute of Applied Sciences in Lyon, France, in 2004 and the Ph.D. degree with honors in electrical engineering from the Ecole Centrale de Lyon, France, in 2007. From 2004 to 2014 he was with the R&D Section of EDF, working on the simulation and analysis of electromagnetic transients. He was also in charge of the technical coordination of the Electromagnetic Transient Program (EMTP) for EDF. From 2014 to 2020, he led a team of around 20 highly skilled engineers and PhDs on Power Systems and grid connection for EDF. He is currently with Enedis, where he is in charge of DSO/TSO coordination, while also serving as an expert in demand-side flexibility mechanisms.

Benoit Bouzigon received an engineering degree in electronics and communications from École Nationale d'Ingénieurs de Brest, France, and an M.S. degree in telecommunications from École nationale supérieure des télécommunications de Bretagne (Télécom Bretagne), France, in 2004. He also received an engineering degree in energy systems from CentraleSupélec, France, in 2006. He began his career in the EDF group in 2007 as a Dispatcher and then as Team Manager for the Normandy Paris transmission network, before joining Enedis in the position of Supply Chain Manager for the Occitanie region. Currently, he is the deputy director in charge of Customers and Territories of the Centre Val de Loire region.